Journal of Materials and Environmental Sciences
ISSN : 2028-2508
CODEN : JMESCN

J. Mater. Environ. Sci., 2019, Volume 10, Issue 2, Page 141-162

http://www.jmaterenvironsci.com

Anti-Corrosion Nickel/Reduced Graphene Oxide-Titanium Dioxide Coating for Mild Steel in Organic Acids

Kh. El-Sayed[a,d], Z. Abdel Hamid[b], Taher A. Salah Eldin[a,d], H. B. Hassan[c]

[a] *Nanotechnology & Advanced Materials Central Lab, Agriculture Research Center, Giza, Egypt.*
[b] *Corrosion Control and Surface Protection Laboratory, CMRDI, Helwan, Cairo, Egypt.*
[c] *Faculty of science, Cairo University, Giza, Egypt.*
[d] *Nanotechnology Research Center, British University in Egypt.*

Received 26 March 2019,
Revised 1 May 2019,
Accepted 2 May 2019

Keywords

- ✓ Anticorrosion;
- ✓ Graphene;
- ✓ Nanocomposite;
- ✓ Electrodeposition;
- ✓ Tafel;
- ✓ EIS.

forzeinab@yahoo.com
Tel.:+201223405792;
Fax: +20 25010639

Abstract

As long as the mild steel is used in building structure in many industries because of its advantages, this study will introduce surface enhancement for the mild steel used in agricultural and food industries. In this study, Nickel–reduced graphene oxide–titanium dioxide (Ni–RGO–TiO_2) coatings were prepared on mild steel by electrodeposition of a hydrothermally synthesized grapheme –TiO_2 nanocomposite The RGO–TiO_2 nanocomposite size and formation was characterized using different techniques such as X-ray diffraction, Transmission electron microscopy, Raman spectroscopy and X-ray photoelectron spectroscopy. The surface morphology and composition of the Ni–RGO–TiO_2 coating were evaluated by scanning electron microscopy and energy dispersive X-ray spectroscopy. The influence of the RGO–TiO_2 content in the coatings on the anti-corrosion behavior of the coating layer was evaluated in 0.06 M citric acid and 0.1 M acetic acid. Electrochemical measurements revealed that a Ni/nanocomposite layer containing 20.4 wt.% RGO–TiO_2substantially enhanced the corrosion resistance of mild steel compared to a Ni coating. In 0.06 M citric acid and 0.1 M acetic acid, the Ni/RGO–TiO_2-coated mild steel displayed lower corrosion rates (0.148 and 0.189 mm/y, respectively) than bare mild steel (4.252 and 1.41 mm/y, respectively).

1. Introduction

Corrosion, which results from electrochemical reactions or the chemical decomposition of the metal components of a building, can cause major industrial problems, including the sudden collapse of metal buildings. Various techniques, such as removing the oxidizing material or oxygen, covering the metal surface with a layer of anticorrosion material, or controlling the environment, have been used to prevent or delay corrosion. Small amounts of corrosion inhibitor can also reduce the corrosion rate in a corrosive environment [1].

Mild steel, which is the most common structural steel, is useful for building a wide variety of structures, such as boats, docks, vessels, water pipes, tanks, and silos. Its frequent use stems from its ready availability and low price in addition to its processability. Specifically, it is a very hard and durable material which is easy to weld and anneal. However, It readily corrodes in all environments [2], which restricts its use in acidic media.. Citric acid, formic acid, and acetic acid are considered the most important organic acids in several fields ranging from the paper and pharmaceutical sectors to the textile and petrochemical industries[3]. Pure acetic acid and citric acid are slightly less corrosive than acid mixtures but strongly affect corrosion systems [4, 5].

Different methods, such as applying different types of coatings and inhibitors, can be employed to protect mild steel from corrosion [6, 7]. Specifically, coatings have received considerable attention because they can isolate the coated metal from the surrounding environment and improve substrate surface quality [7-10]. Metallic coatings can preserve the aesthetics and decorative finish of a material as well as inhibit corrosion. They can be applied through different techniques, such as electroplating, hot dipping, physical vapor deposition,

electroless plating, and chemical vapor deposition [11]. Electrodeposition benefits from many advantages, such as low energy requirements, low cost, uniform deposition, precise control, good reproducibility, and high production rate [12]. Moreover, this widely used technique can produce nanocomposites and nanocrystalline coatings at room temperature [13]. Electrodeposited composite coatings enhance the physical and mechanical properties of the coated substrate, such as their wear and corrosion resistance, compared to their pure metal analogues. This enhancement depends on the content and properties of the co-deposited particles [14-18]. The incorporation of nanoparticles, such as CuO, SiO_2, ZrO_2, TiO_2, and ZnO, as reinforcements into the coating layer can improve the properties of the material [7,13,15,18,19].

Carbon nanostructured materials have recently prompted tremendous interest in both applied and fundamental research [20, 21] because their exceptional properties make them suitable for many applications, such as energy storage systems, electrochemical oriented electrodes, coatings, and composite-based reinforcements [22-25]. In particular, graphene, which is stabilized by the honeycomb configuration of its sp^2 carbon atoms, benefits from thermal, chemical, and mechanical properties that can enhance the properties and versatility of other materials[7, 22].It acts as a substrate for nanoparticles for generating graphene-based nanocomposites, which gives rise to novel properties that depend on the nanoparticle composition. In recent years, the combination of graphene with metallic nanoparticles has produced nanocomposites with promising magnetic, catalytic, and optoelectronic properties. These graphene nanocomposites integrate specific properties associated with the nanoparticles, such as electrical conductivity, catalytic activity, and corrosion protection [26-28].

The electrodeposition of nickel (Ni) imparts corrosion resistance to materials in weakly alkaline and acidic environments in addition to improved microhardness and tribological properties [29]. Incorporating a graphene nanocomposite into a Ni matrix to produce a Ni-graphene nanocomposite is important for nanocomposite electrodeposition because graphene possesses properties that make it suitable for corrosion protection [7, 30].

Here, we prepare a Ni-reduced graphene oxide-titanium dioxide (Ni/RGO–TiO_2) coating by electrodeposition and investigate its corrosion behavior in different organic acid media,such as citric acid and acetic acid, chosen due to their industrial significance.

2. Material and methods

Nanomaterial preparation

Graphene oxide (GO) was fabricated according to the modified Hummer's method that was discussed briefly in the literature [7, 31] using Alfa Aesar natural graphite powder (99.9995%), Sigma-Aldrich sulfuric acid (H_2SO_4, 95-97%) and sodium nitrate ($NaNO_3$), analytical grade potassium permanganate ($KMnO_4$) and Alpha Chemika hydrogen peroxide (30% H_2O_2). RGO-TiO_2 was prepared by following the procedures in the previous study using Sigma-Aldrich Ti(IV) isopropoxide (TTIP) [$Ti(OCH(CH3)_2)_4$] (99.99%) [7].

Electrodeposition process

Coatings were obtained on mild steel substrates as the cathode with dimensions of 50 × 40 × 0.6 mm and a composition of C, 0.15%; Mn, 0.6%; P, 0.028%; and Si, 0.25% balanced with Fe. An electrodeposition technique was used to prepare Ni and its composite coatings. The chemical composition of the Ni bath was $NiSO_4.7H_2O$ [26.26 gL^{-1}], Na_2SO_4 [56.81 gL^{-1}], H_3BO_3 [18.54 gL^{-1}], and the RGO-TiO_2 reinforcement material with different concentrations [0–1gL^{-1}]. The operating conditions were as follows: current density, 2.5–20 $mAcm^{-2}$; temperature, 30 °C; pH, 5 (adjusted using an ammonia solution and sulfuric acid, 10%); deposition time, 60 min; and stirring speed, 150 rpm. Before the electrodeposition process, the mild steel surface was subjected to many pretreatment processes. The first step was a mechanical treatment, in which several grades of emery paper were used until a sleek surface was obtained. The second pretreatment step was degreasing, in which an alkaline solution consisting of NaOH, Na_2CO_3 and Na_3PO_4 at 70 °C was used to remove grease and oil by immersing the sample in the solution for 5 min at 70 °C. After every step, the sample was washed with deionized water then dried. Before the electrodeposition of RGO-TiO_2, the deposition solution containing RGO-TiO_2 was stirred for 5 h to ensure homogeneity and a good dispersion of RGO-TiO_2 nanoparticles in the solution.

2. Characterization techniques

Nanomaterial characterization techniques

All the nanomaterial samples were evaluated by X-ray diffraction (XRD) using a PANalyticalX'Pert PRO instrument (Cu Kα radiation (λ = 1.5404 Å)), transmission electron microscopy (TEM) using a Tecnai G2 20S-Twin (200 kV), X-ray photoelectron spectroscopy (XPS) using a Thermo Scientific K-Alpha instrument with an Al Kα monochromatic X-ray source, and Raman spectroscopy using an HR UV 800 confocal scanning spectrometer (Horiba JobinYvon) at room temperature.

Coating layer characterization

The morphologies of the coatings surface were inspected using a field emission scanning electron microscope (FE-SEM, model Quanta FEI), and elemental analysis of the coating layer was performed using an energy dispersive X-ray (EDX) unit attached to the instrument.

Corrosion tests

Tafel line and electrochemical impedance spectroscopy (EIS) measurements were utilized to review the corrosion performance of the prepared samples in 0.06 M citric acid and 0.1 M acetic acid. The electrochemical measurements were implemented in a three-electrode cell consisting of a $Hg/Hg_2Cl_2/Cl^-$ electrode with E° = 240 mV vs. standard hydrogen electrode (SHE) as the reference electrode, a platinum sheet as the auxiliary electrode and the electrodeposited sample (Ni/mild steel, Ni-RGO-TiO_2/mild steel and bare mild steel) with a reveal surface area of 1 cm^2 as the working electrode. The experiment was performed in aerated solution at 25 °C. The electrodes were immersed in the electrolyte (0.06 M citric acid and 0.1 M acetic acid) for nearly 30 min until the open circuit potential (E_{corr}) was achieved. Polarization was started from the E_{corr} value down to –500 mV in the cathodic direction and then reversed in the anodic direction from the E_{corr} value up to +500 mV. The corrosion current (I_{corr}) was calculated from the intersection, at zero polarization, of the linear portion of the anodic and cathodic curves. The EIS measurements were performed in the frequency range of 35–100 mHz with a 10 mV sinusoidal potential using AC signals at E_{corr}.

3. Results and discussion

Nanoparticle and nanocomposite characterization

In this section, the advanced techniques have been used in order to confirm the formation of nanoparticle and nanocomposite. Figure 1 depicts TEM micrographs of the prepared graphene oxide (GO) sheets, TiO_2, and RGO–TiO_2 samples. Figure 1(a) shows that GO sheets comprised several layers stacked on top of each other. The spherical TiO_2 nanoparticles, which measured 5 to 10 nm in diameter (Figure 1(b)), formed well-dispersed but somewhat agglomerated RGO–TiO_2 composite structures across the nanosheets(Figure 1(c)). The selected area electron diffraction (SAED) pattern of the composite (Inset, Figure 1(c)) was consistent with the diffraction pattern of TiO_2 nanoparticles. The high-resolution TEM (HRTEM) image (Figure 1(d)) displays a lattice indicative of highly crystalline TiO_2, whose d-spacing parameter measured 3.51 Å. This d-spacing value corresponds to the (101) lattice plane of TiO_2. The EDX spectrum of the composite (Figure 1(e)) reveals the presence of Ti, O, Cu, and a high percentage of C in the sample. The Cu and high percentage of C arise from the TEM grid; thus, these components can be excluded from the results. Overall, therefore, no chemical impurity was detected in the sample.

Figure 2(a) shows the XRD patterns of RGO, RGO–TiO_2, and TiO_2 along with the pattern for GO (inset), which presents a peak corresponding to the (001) plane of GO at 11.7° [7]. The XRD pattern of RGO displayed a broad diffraction peak between 24° and 26° corresponding to the (002) plane, and no peak characteristic of GO at 11.7°, confirming that the hydrothermal treatment removed the epoxide and hydroxyl functional groups from the GO sheets. The patterns obtained for RGO–TiO_2 and TiO_2 showed peaks that corresponded to the crystallographic reflections of the (101), (004), (200), (105), (211), (204), (116), (220), and (215) planes and matched the peaks on the standard anatase TiO_2card (JCPDS 01-75-2547). Additionally, no diffraction peaks were observed for RGO between 24° and 26° in RGO–TiO_2, which suggests that the intense peak detected at 25.3° for the (101) plane of anatase TiO_2 shielded the peak corresponding to the (002) plane of RGO.

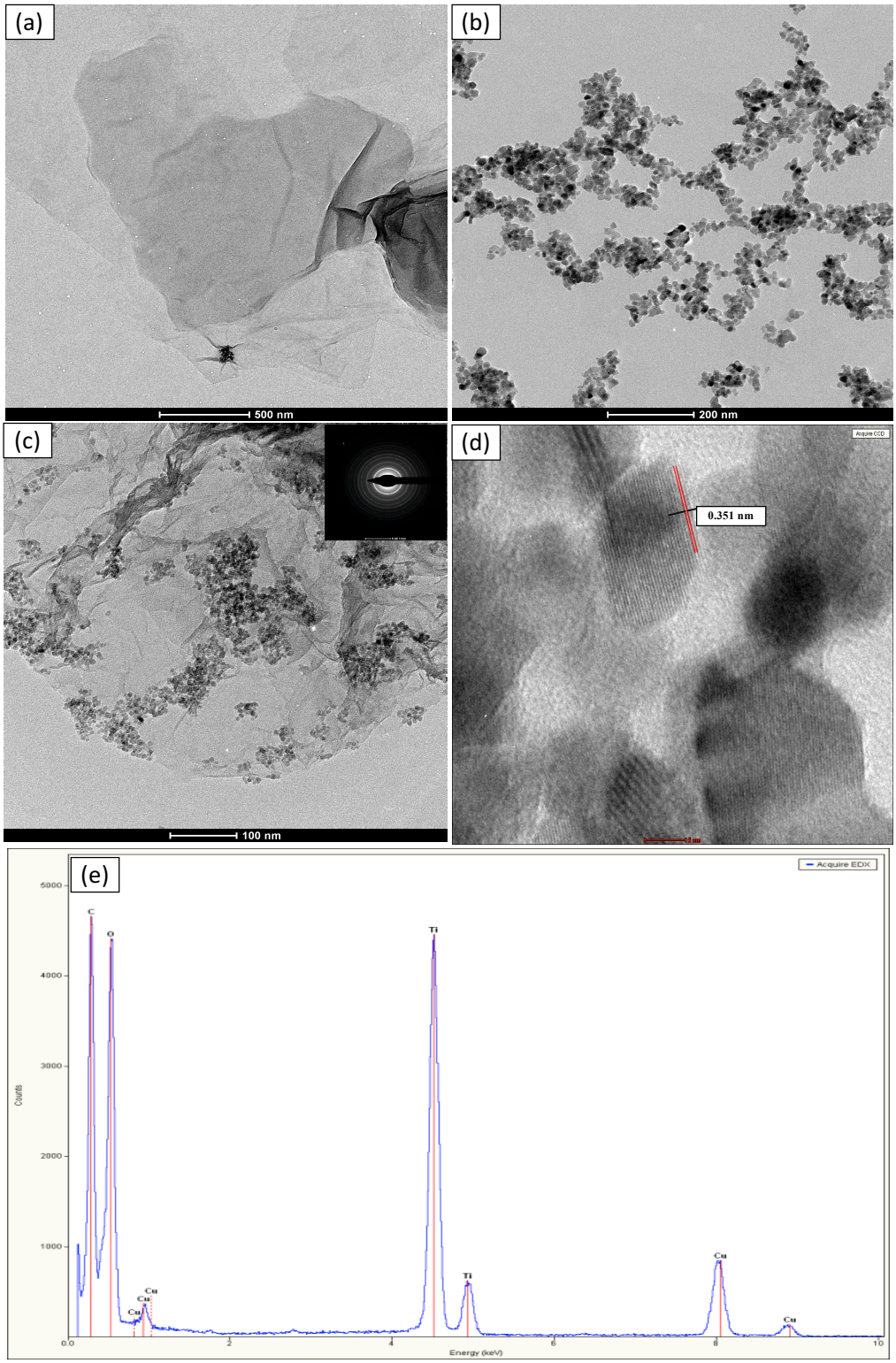

Figure 1. Typical reduced graphene oxide TEM image (a), TiO_2 anatase TEM image (b), reduced graphene oxide-TiO_2 composite TEM image and in sit SAED image (c), High resolution TEM image for TiO_2(d) and EDX for the composite (e).

The samples were examined by Raman spectroscopy, a non-destructive characterization tool for carbonaceous materials that has proven especially effective for distinguishing the ordered and disordered crystal structures of carbon. Figure 2(b) shows the Raman spectra of GO, RGO, RGO–TiO_2, and TiO_2. The Raman spectrum of GO exhibited D and G spectral bands characteristic of graphene at 1355 and 1600 cm^{-1}, respectively. The D band indicates the presence of disordered carbon, generally in the form of sp^3 defects, and

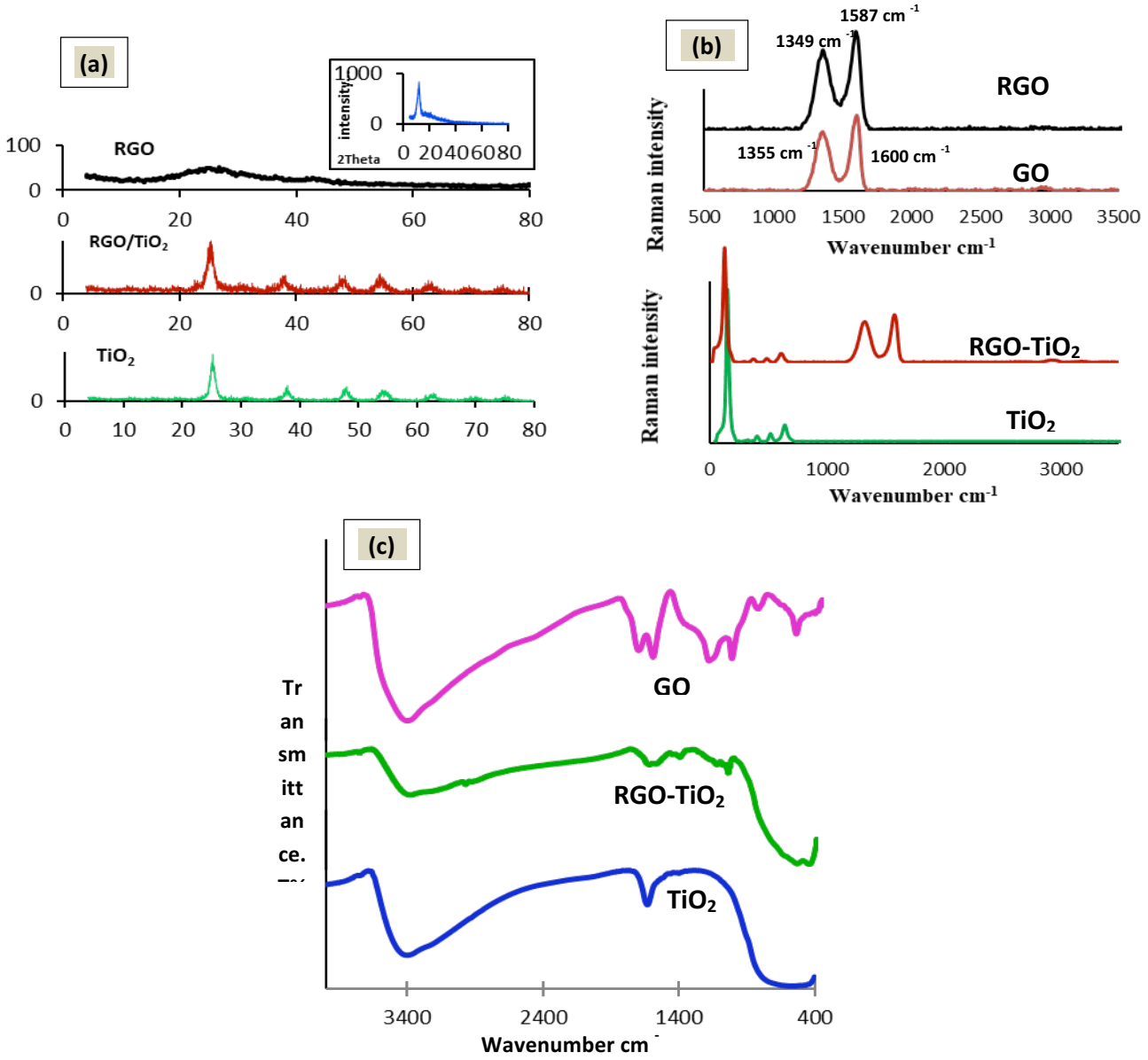

Figure 2.(a) XRD pattern for RGO, RGO-TiO_2, TiO_2 and in sit image for GO. (b) Raman spectrum for GO, RGO, RGO-TiO_2 and TiO_2. (c) FTIR spectrum for GO, RGO-TiO_2 and anatase TiO_2.

the G band provides information about the in-plane vibrations of sp^2-bonded carbon atoms in a two-dimensional hexagonal lattice [32]. Therefore, the intensity D band observed for GO is consistent with a high density of defects and structural disorder [33]. For RGO, the D and G bands appeared at 1349 and 1587 cm^{-1},which represents a slight red shift compared to GO, confirming the reduction of GO[32]. The ratio between the D and G band intensities (I_D/I_G) is an indicator of the number of defects and the degree of structural disorder [33, 34]. The I_D/I_G ratio amounted to 0.77 for GO, which is slightly lower than for RGO (I_D/I_G = 0.81). This finding indicates an increase in crystal disorder in RGO because of the hydrothermal treatment and reduction reaction[35]. The Raman spectrum of pure TiO_2 (Figure 2(b)) contains peaks that were ascribed to the anatase phase at approximately 151, 404, 517, and 641 cm^{-1}. These peaks were also observed in the Raman spectrum of RGO-TiO_2, suggesting that the anatase TiO_2 crystallites are the major species [36].

Two bands at approximately 1349 (D band) and 1591 cm^{-1} (G band) were also clearly observed for the graphitized structures, proving the presence of graphene [37]. Moreover, RGO–TiO_2presented slightly shifted D and G bands compared to those of GO (1355 and 1596 cm^{-1}, respectively), consistent with the reduction of GO. They exhibited a greater I_D/I_G value (1.19) than GO (0.77), which indicates the presence of more localized sp^3 defects within their sp^2 carbon network [38]. This also suggests that the TiO_2 lattice was entrapped inside the graphene sheets through the concurrent chemical reaction and sonication assistance [39].

Figure 2(c) shows the FTIR spectra of GO, RGO, and anatase TiO_2. The FTIR spectrum of GO displayed peaks at 1053, 1220, 1625, 1729, and 3433 cm^{-1}, which represented the stretching of C–O, C–OH, C–C, C–O, and O–H bonds, respectively, in oxygen-containing functional groups [7, 40]. These peaks showed a sharp decrease in the spectrum of RGO–TiO_2, confirming the reduction of GO during the hydrothermal treatment. For anatase TiO_2, three peaks appeared at 499, 1630, and 3397 cm^{-1}, which were assigned to Ti–O–Ti bond stretching vibrations [41]. In addition to a peak at 1616 cm^{-1} corresponding to the C–C bond stretchingin the graphene skeleton, the spectrum of RGO-TiO_2 presented a strong band at 558 cm^{-1}, which was attributed to Ti–O–C bond vibrations. This confirmed that the anatase TiO_2 nanoparticles were anchored on the graphene sheet surface.

The chemical composition and binding environment of the composite were further evaluated by XPS analysis (Figure 3). Figure 3(a) shows survey scans for GO and RGO–TiO_2. The survey spectrum of GO showed two peaks at 285.9 and 533.3 eV, assigned to C 1s and O 1s, respectively. A new peak appeared at 460.2 eV for RGO–TiO_2, which were attributed to Ti 2p [42]. The high-resolution C 1s spectrum of GO (Figure 3(b)) displayed three distinct peaks at 284.7, 286.9, and 288.7 eV corresponding to C–C bonds, C–O bonds of epoxy and hydroxy groups, and C=O bond of carbonyl groups, respectively [7, 43]. All three peaks were detected at the same positions forRGO–TiO_2, (Figure 3(c)) but the peaks observed at 286.9 and 288.7 eV presented dramatically lower intensities than for GO

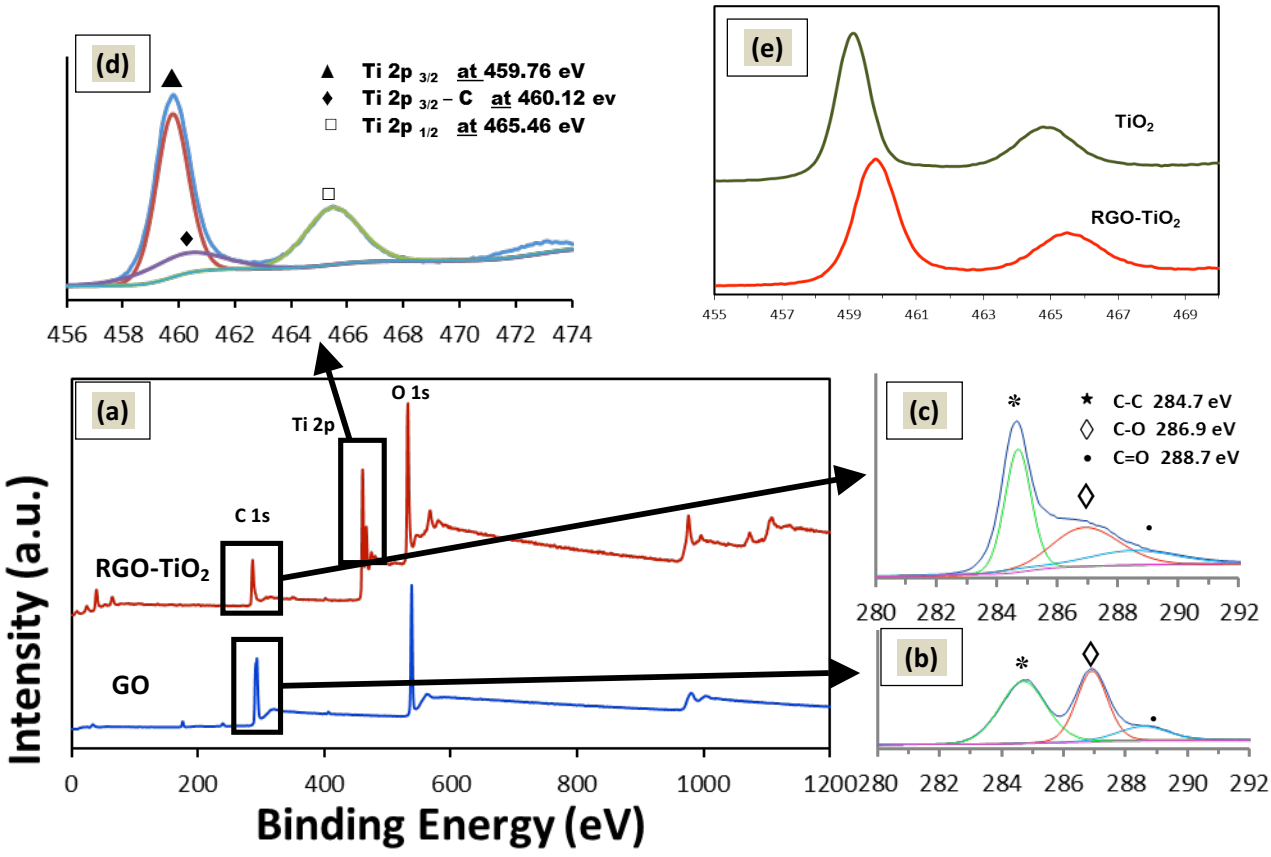

Figure 3. (a) XPS survey of GO and RGO–TiO_2. High resolution XPS Spectra of C 1s for (b) GO and (C) RGO–TiO_2. (d) High resolution XPS Spectra of Ti 2p for RGO-TiO_2. (e) Ti 2p XPS spectra of RGO–TiO_2 and pure TiO_2.

(Figure 3(b)). This indicates that the hydrothermal process eliminated most oxygen-containing species from the GO sheets, in agreement with the FTIR results. The high-resolution Ti 2p spectrum of RGO–TiO_2 (Figure 3(d)) displayed two characteristic peaks of TiO_2 are observed at 459.7 (Ti $2p_{3/2}$) and 465.4 eV (Ti $2p_{1/2}$) in addition to a peak at 460.1 eV attributed to the Ti–C bonds between graphene and TiO_2 [44]. Spin-orbit splitting in the Ti 2p spectrum showed peaks at 459.18 (Ti $2p_{3/2}$) and 464.88eV (Ti $2p_{1/2}$) for pure TiO_2. It led to peaks at 459.76 (Ti $2p_{3/2}$) and 465.46 eV (Ti $2p_{1/2}$) for TiO_2 in the RGO–TiO_2 composite (Figure 3(e)), revealing a substantial

red shift in the peaks relative to those of pure TiO_2. This shift indicates either the presence of electronic interactions between TiO_2 and graphene sheet or a change in chemical state [7, 45].

Coating layer characterization

Figures 4(a) and (c) shows the coating surface morphologies of Ni–20.4 wt.% RGO–TiO_2, which was obtained by incorporating the 0.4 g L^{-1} RGO–TiO_2 nanocomposite in the coating bath, and pure Ni, respectively, as described in our previous work [7]. Adding the RGO–TiO_2 nanocomposite clearly affected the Ni particle size and shape as well as compactness in the coating.

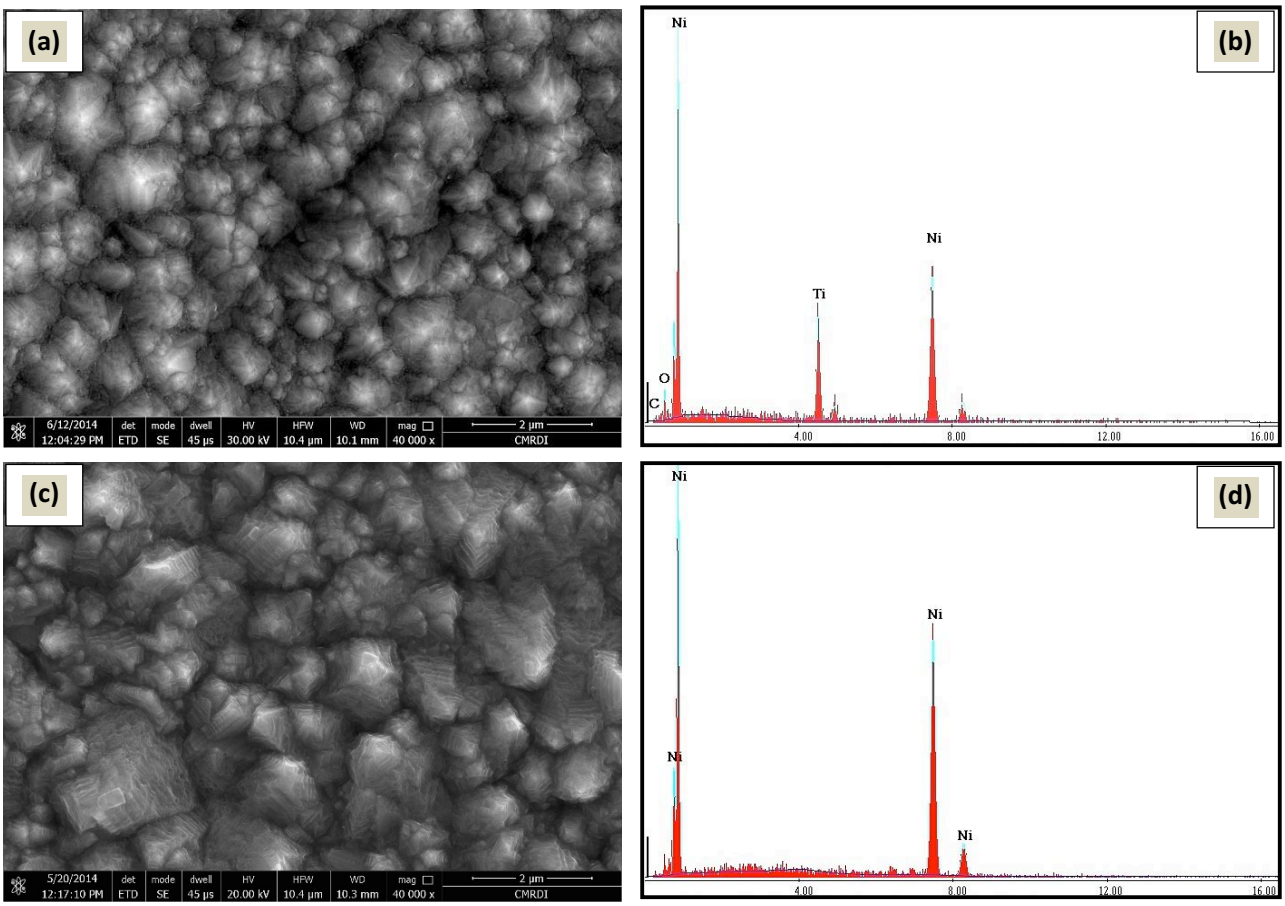

Figure 4. FESEM image for (a) mild steel coated with Ni-RGO-TiO_2 (0.4 g L^{-1} RGO-TiO_2), (c) mild steel coated with Ni only. EDX spectrum for (b) Ni-RGO-TiO_2 coating film, (d) Ni coating film.

The Ni coating formed a cubic crystal structure (Figure 4(c)), while the Ni–20.4 wt.% RGO–TiO_2 nanocomposite surface adopteda particulate-like structure consisting of finer grains and a more compact film (Figure 4(a)). The RGO–TiO_2 nanocomposite-induced decrease in Ni particle size may arise from the adsorption of RGO–TiO_2 particles onto the Ni grains, which restricts the growth of these grains to small and fine particles [7]. Furthermore, the incorporation of RGO–TiO_2 within the Ni coating was confirmed by EDX (Figures 4(b) and 4(d)).

Corrosion tests in 0.06 M citric acid

Polarization Tafel lines of bare and coated mild steel electrodes in 0.06 M citric acid

The polarization profiles of mild steel electrodes coated with Ni alone or in mixtures containing different RGO–TiO2concentrations in 0.06 M citric acid were compared with that of bare electrodes (Figure 5).The corresponding electrochemical parameters, including the corrosion current density (I_{corr}), corrosion potential (E_{corr}), cathodic (b_c) and anodic Tafel slopes (b_a), and corrosion rate (in mm/y), are listed in Table 1. The Ni–20.4 wt.% RGO–TiO2coating obtained at a current density of 10 mA cm-2displayed the lowest corrosion rate.

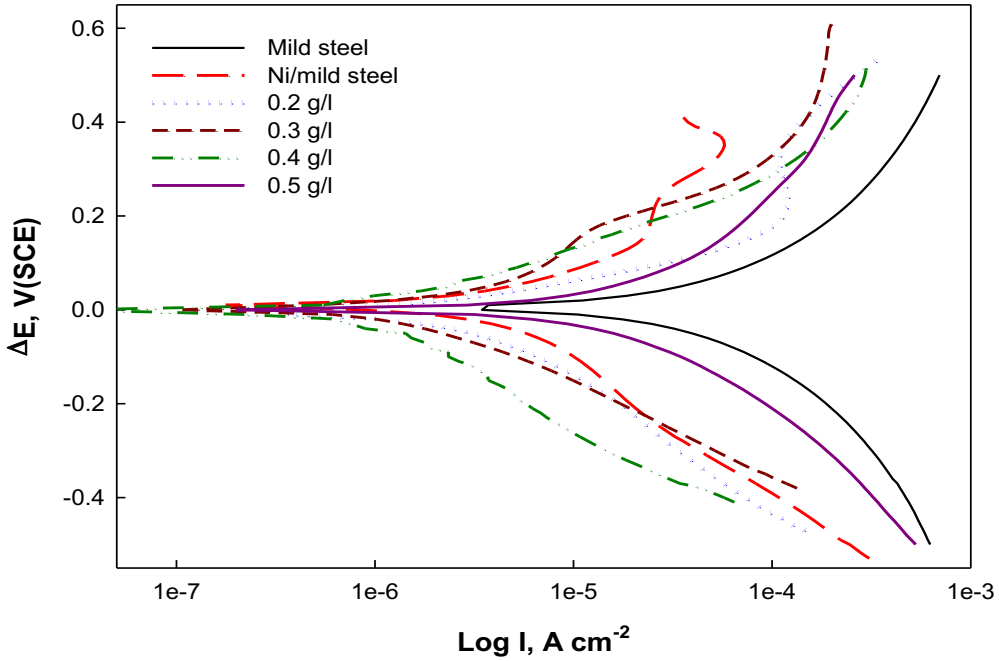

Figure 5. Polarization Tafel lines of mild steel, Ni/mild steel and Ni-RGO-TiO_2/mild steel electrodes (prepared at different concentration of RGO-TiO_2 nanocomposite) in 0.06 M citric acid solution.

Table 1. Electrochemical parameters derived from Tafel lines for mild steel, electrodeposited Ni/ mild steel and Ni-RGO-TiO_2/mild steel containing different concentration of RGO-TiO_2 nanocomposite (deposited at 10 mA cm^{-2}) in 0.06 M citric acid at 25 °C

Sample	RGO-TiO_2 in the bath, g L^{-1}	E_{corr}, V (SCE)	I_{corr}, (A/cm^2)	b_a (V/dec)	$-b_c$ (V/dec)	C. R. mm/y
Mild Steel	-	**-0.578**	**7.222×10^{-5}**	**0.447**	**0.465**	**4.252**
Ni/mild steel	-	**-0.282**	**5.917×10^{-6}**	**0.429**	**0.266**	**0.348**
Ni-RGO-TiO_2 (I)	**0.2**	**-0.064**	**8.131×10^{-5}**	**0.470**	**0.322**	**4.789**
Ni-RGO-TiO_2 (II)	**0.3**	**-0.079**	**4.05×10^{-6}**	**0.304**	**0.208**	**0.238**
Ni-RGO-TiO_2 (III)	**0.4**	**-0.144**	**2.52×10^{-6}**	**0.259**	**0.255**	**0.148**
Ni-RGO-TiO_2 (IV)	**0.5**	**-0.387**	**2.638×10^{-5}**	**0.452**	**0.344**	**1.554**

This result can be attributed to stem from the somewhat compact and defect-free surface morphology which exhibits a good distribution and high RGO–TiO_2 content.

Figure 6 and **Table 2** show the effect of citric acid concentration on the Tafel lines of Ni–20.4 wt.%RGO–TiO_2-coated mild steel prepared at 10 mA cm^{-2}. An increase in the citric acid concentration up to 0.06 M shifted the polarization curve toward a lower polarization current density. Above this concentration, the corrosion current increased. These results indicate that low citric acid concentrations have some inhibitory effects on the electrode surface. The decrease in the corrosion rate may arise from the presence of the protective coating barrier and the adsorption of citric acid molecules onto the electrode surface.

The potentiodynamic Tafel plots of Ni–20.4 wt.% RGO–TiO_2-coated electrodes prepared at different deposition current densities in 0.06 M citric acid are shown in **Figure 7**, and the derived electrochemical parameters are listed in **Table 3.** The Tafel lines shifted toward a lower polarization current with increasing deposition current. Moreover, the Ni–RGO–TiO_2-coated electrode prepared at 10 mA cm^{-2} exhibited the lowest corrosion rate. This result may arise from the defect-free coating morphology at high RGO–TiO_2content, which protected the surface from corrosion.

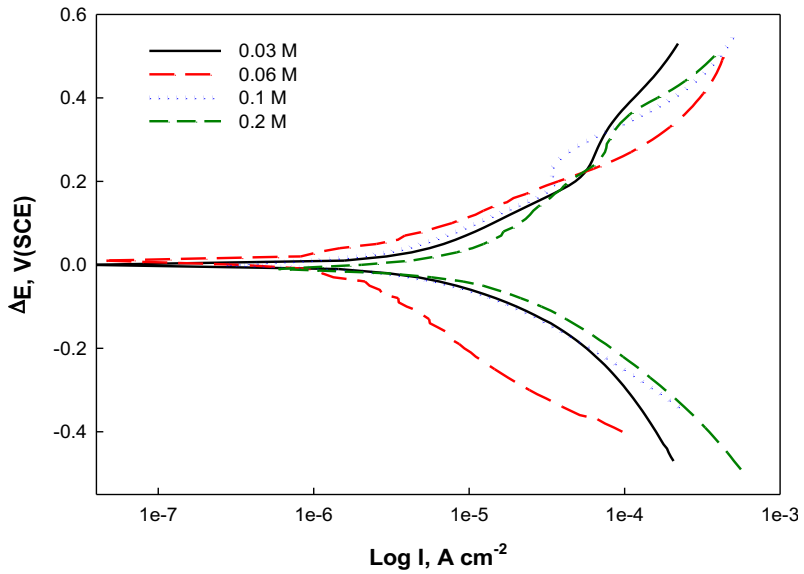

Figure 6. Polarization Tafel lines of Ni-RGO-TiO_2/mild steel (prepared at 10 mA cm^{-2} and 0.4 g L^{-1} RGO -TiO_2) in different concentration of citric acid solution.

Table 2. Electrochemical parameters derived from Tafel lines of Ni- RGO -TiO_2/mild steel (prepared at 10 mA cm^{-2} and 0.4 g L^{-1} RGO -TiO_2) in different concentrations of citric acid

Citric acid concentration, M	$E_{corr,}$ V (SCE)	$I_{corr,}$ A cm^{-2}	$b_{a,}$ V dec^{-1}	$-b_{c,}$ V dec^{-1}	C.R mm/y
0.03	**-0.292**	**1.87 x10^{-5}**	**0.533**	**0.391**	**0.199**
0.06	**-0.144**	**2.52× 10^{-6}**	**0.259**	**0.255**	**0.148**
0.1	**-0.178**	**4.58 x10^{-6}**	**0.224**	**0.218**	**0.435**
0.2	**-0.346**	**1.65x10^{-5}**	**0.418**	**0.303**	**1.57**

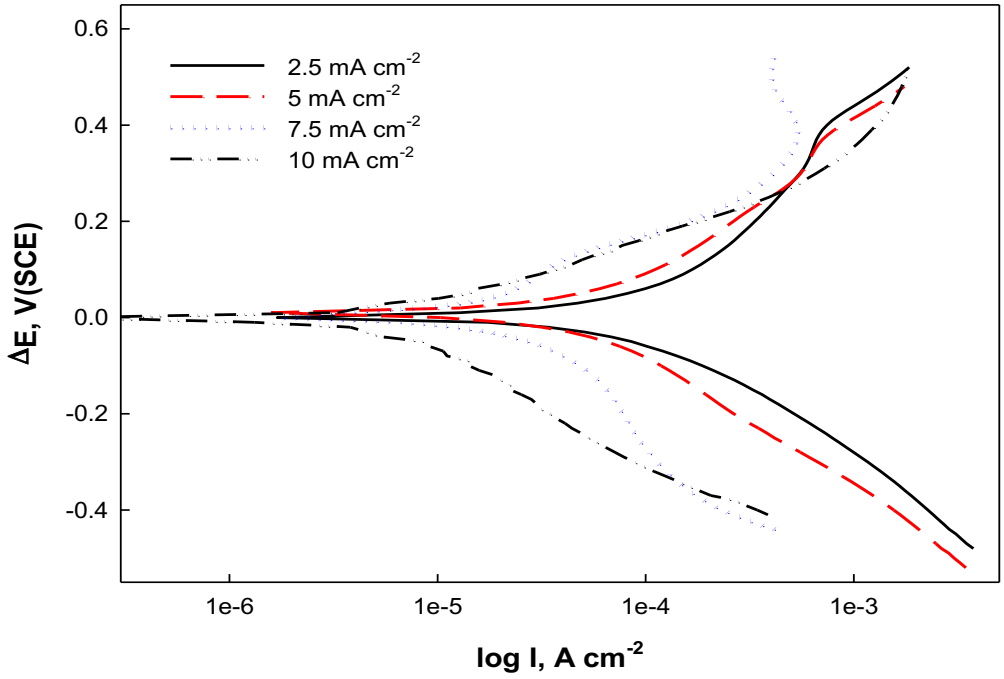

Figure 7. Polarization Tafel lines of Ni- RGO -TiO_2/mild steel (prepared at different current densities and 0.4 g L^{-1} RGO -TiO_2) in 0.06 M citric acid solution.

Table 3. Electrochemical parameters derived from Tafel lines of Ni- RGO -TiO_2/mild steel (prepared at different deposition current densities and 0.4 g L^{-1} RGO -TiO_2) in 0.06 M citric acid

Sample at cd (mA cm^{-2})	E_{corr}, V (SCE)	I_{corr}, A cm^{-2}	b_a, V dec^{-1}	$-b_c$, V dec^{-1}	C.R mm/y
2.5	**-0.365**	**$1.35x10^{-5}$**	**0.562**	**0.92**	**1.28**
5	**-0.386**	**$5.95 x10^{-6}$**	**0.353**	**0.256**	**0.564**
7.5	**-0.088**	**$0.45x10^{-5}$**	**0.413**	**0.589**	**0.435**
10	**-0.144**	**2.52×10^{-6}**	**0.259**	**0.255**	**0.148**

Electrochemical impedance spectroscopy in 0.06 M citric acid

The corrosion resistance of bare and coated steel electrodes prepared with different concentrations of RGO-$TiO_2$was assessed by electrochemical impedance spectroscopy (EIS) (**Figures 8 and 9** and **Tables 4 and 5**). These measurements were performed in 0.06 M citric acid for applied frequencies ranging from 35 kHz to 100 MHz. The resulting Nyquist plots displayed a straight (Warburg) line in the low-frequency region and a capacitive loop at high frequency (**Figures 8 and 9**).The Warburg impedance (W) results from the propagation of the cathodic and anodic reaction products from the solution to the electrode surface and ensures that the surface protective coating restricts mass transport. On the other hand, the capacitive loop originates from charge transfer resistance (R_{ct}).

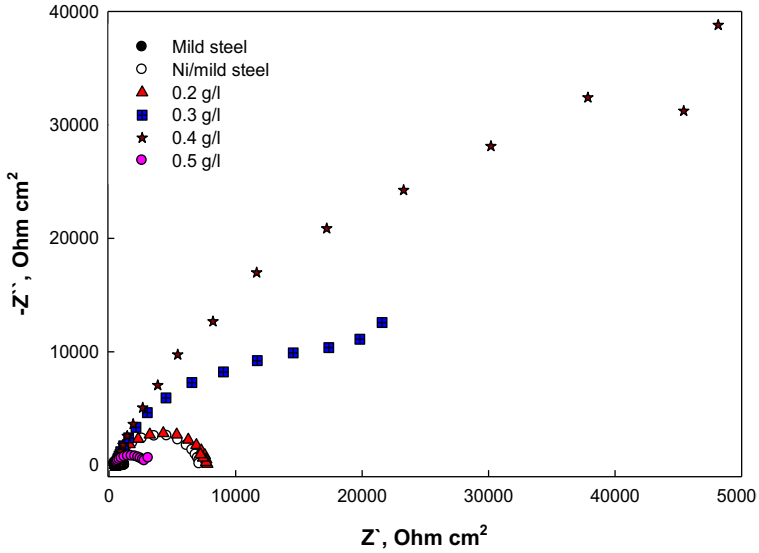

Figure 8. Nyquist plots for mild steel, Ni/mild steel and Ni-RGO-TiO_2/mild steel electrodes (prepared at different RGO-TiO_2 concentrations and at 10 mA cm^{-2}) in 0.06 M citric acid at open circuit potential.

Table 4. Electrochemical parameters derived from EIS for mild steel, Ni/mild steel and Ni- RGO -TiO_2/mild steel (prepared at different RGO -TiO_2 nanocomposite concentrations in the bath and 10 mA cm^{-2}) in 0.06 M citric acid at 25 °C

Sample	Wt. % of RGO -TiO_2 in the coating layer	R_s, Ohm cm^2	R_p, Ohm cm^2	C, F cm^{-2}	W Ohm cm^2	n
Mild steel	-	**$5.72x10^{-2}$**	**$6.27x10^{2}$**	**$5.22x10^{-5}$**	**2.893**	**0.98**
Ni/mild steel	-	**$6.98x10^{2}$**	**$6.11x10^{3}$**	**$2.9x10^{-5}$**	**4.2x10**	**0.97**
Ni– RGO –TiO_2 (I)	**17.48**	**$6.39x10^{2}$**	**$6.96x10^{3}$**	**$2.18x10^{-5}$**	**$1.03x10^{2}$**	**0.97**
Ni– RGO –TiO_2 (II)	**18.67**	**$6.7x10^{2}$**	**$1.25x10^{4}$**	**$7.1x10^{-5}$**	**$2.85x10^{3}$**	**0.96**
Ni– RGO –TiO_2 (III)	**20.43**	**$1.82x10^{3}$**	**$6.40x10^{4}$**	**$8.48x10^{-5}$**	**$8.48x10^{-5}$**	**0.95**
Ni– RGO –TiO_2 (IV)	**19.32**	**$5.43x10^{2}$**	**$2.21x10^{3}$**	**$9.62x10^{-5}$**	**1.58x10**	**0.98**

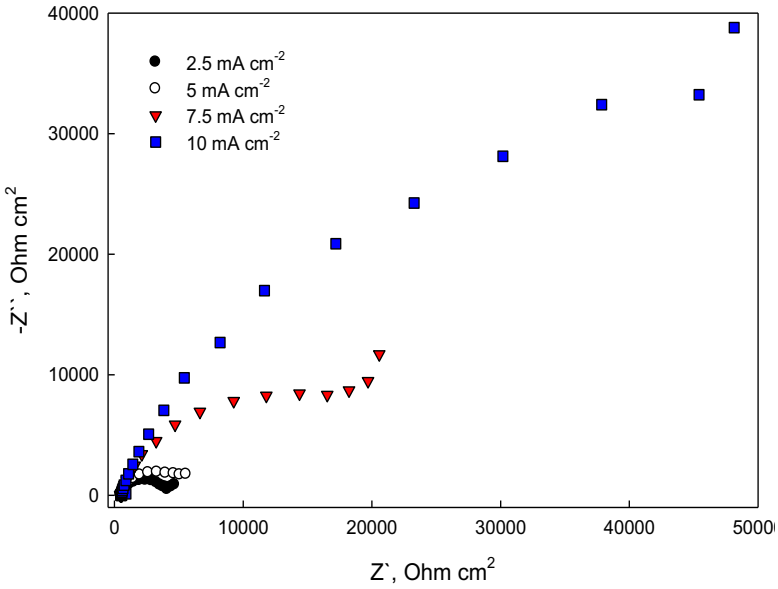

Figure 9. Nyquist plots for Ni-RGO-TiO_2/mild steel electrodes (prepared at different deposition current densities and 0.4 g L^{-1} RGO-TiO_2) in 0.06 M citric acid at open circuit potential.

Table 5. Electrochemical parameters derived from EIS for Ni- RGO -TiO_2/mild steel (prepared at different deposition current densities and 0.4 g L^{-1} RGO -TiO_2 nanocomposite in the bath) in 0.06 M citric acid at 25 °C

Deposition cd, mA cm^{-2}	R_s, Ohm cm^2	R_p, Ohm cm^2	C, F cm^{-2}	W Ohm cm^2	n
2.5	**$6.4x10^2$**	**$3.18x10^3$**	**$4.32x10^{-5}$**	**$1.25x10^2$**	**0.98**
5	**$6.76x10^2$**	**$5.2x10^3$**	**$3.31x10^{-5}$**	**$2.94x10^2$**	**0.98**
7.5	**$6.5x10^2$**	**$1.24x10^4$**	**$4.52x10^{-5}$**	**$2.61x10^3$**	**0.97**
10	**$1.82x10^3$**	**$6.40x10^4$**	**$8.48x10^{-5}$**	**$8.48x10^{-5}$**	**0.95**

The Ni–RGO–TiO_2-coatedmild steel electrodes exhibited considerably higher polarization resistance (R_p) values than their bare and Ni-coated counterparts. Specifically, the R_p values increased with increasing RGO–TiO_2 nanocomposite content in the coating. They amounted to 0.61, 6.1, and 64 KΩ cm^2 for bare, Ni-coated, and Ni–20.4 wt.% RGO–TiO_2-coated mild steel electrodes, respectively, and achieved their optimum for coatings with a relatively higher RGO–TiO_2 nanocomposite content. Moreover, the corrosion resistance reached a maximum for the Ni–20.4wt.%RGO–TiO_2-coated mild steel electrode, evidence for the high corrosion resistance of the prepared nanocomposite coatings. The decrease in electrolyte penetration into a steel surface results from the presence of these protective coatings and produces a barrier against diffusion. Moreover, an increase in the deposition current density augments R_p values. This electrochemical behavior was represented by the equivalent electrical circuit $R_s(R_pW)C$) (**Figure 10**), where R_s is the resistance created by the solution between the working and reference electrodes, R_p is the corrosion resistance at the metal substrate–solution interface, and C is the capacitive loop.

The R_p values increased with increasing deposition current density (**Figure 9** and **Table 5**) and RGO–TiO_2 concentration in the plating electrolyte. The capacity values of the Ni–RGO–TiO_2-coatedmild steel electrode decreased because of the suitable distribution of the coatings on the electrode, which produced a barrier against diffusion. **Tables 4 and 5** list software-calculated impedance parameters for different composite electrodes. In these tables, the parameter N, whichvaries between 0 and 1, is calculated by the instrument's software to account for deviations from ideal capacitive behavior. It indicates whether the experimental and theoretical impedance parameters of the equivalent model match. The calculated N values show that these results are in good agreement with the data obtained from the Tafel lines.

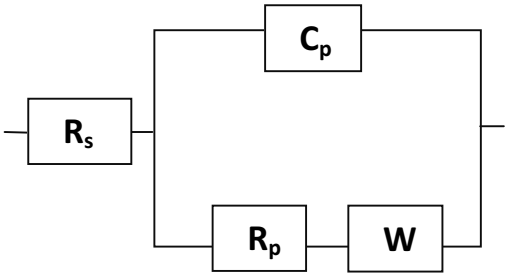

Figure 10. Model of the equivalent circuit represents the corrosion behavior of Ni–RGO–TiO_2/mild steel electrodes in 0.06 M citric acid.

Furthermore, the effect of temperature on the corrosion properties of bare, Ni-coated, and Ni–20.4 wt.%RGO–TiO_2-coatedmild steel electrodes was investigated between 25and 55 °C in 0.06 M citric acid (**Figures 11–13**). The polarization Tafel lines shifted toward higher polarization current and the corrosion current density increased when the temperature rose for all samples. The electrochemical parameters derived from the polarization Tafellines for all samples are summarized in **Tables 6–8**.The corrosion rate can be calculated using:

$$\textbf{Corrosion rate (mm/y)} = 0.00327 \times I_{corr} \times Aw/dn \qquad (1)$$

Where I_{corr} is the corrosion current in microamperes per cm^2, A is the atomic weight of the metal, d is the metal density, and n is the valence of the metal.

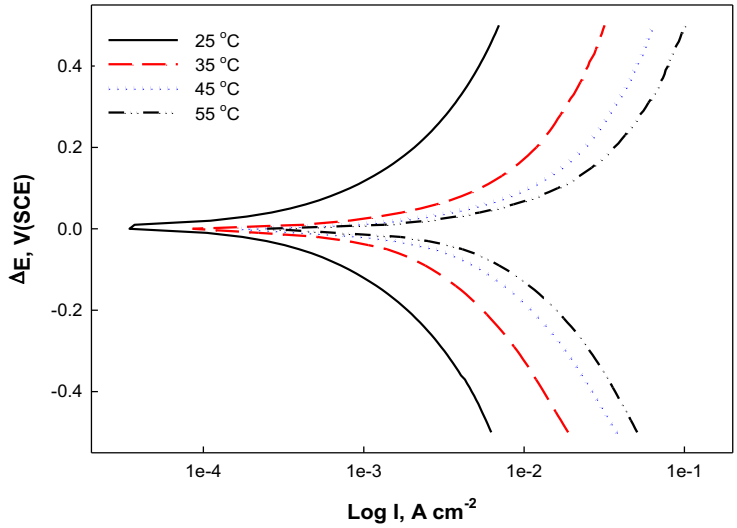

Figure 11. Polarization Tafel lines of mild steel in 0.06 M citric acid solution at different temperatures.

Table 6. Electrochemical parameters derived from Tafel lines for mild steel, at different temperatures in 0.06 M citric acid

Temperature	$E_{corr,}$ V (SCE)	$I_{corr,}$ (A/cm^2)	b_a (V/dec)	$-b_c$ (V/dec)	C. R. mm/y
25°C	**-0.578**	**7.222×10^{-5}**	**0.447**	**0.465**	**4.252**
35°C	**-0.559**	**$6.8x10^{-4}$**	**0.543**	**0.502**	**8.87**
45°C	**-0.556**	**0.0003412**	**0.543**	**0.502**	**25.24**
55°C	**-0.522**	**0.000497**	**0.519**	**0.518**	**29.29**

The corrosion rate increased with temperature in citric acid, which stems from the heat-promoted acceleration of all other corrosion-related processes, such as chemical reactions, electrochemical reactions, and reactive species transfer to the metal surface. Moreover, the Ni–RGO–TiO_2-coated mild steel electrodes displayed lower corrosion rates than their bare and Ni-coated counterparts, which may be attributed to the presence of a protective layer on electrode surfaces.

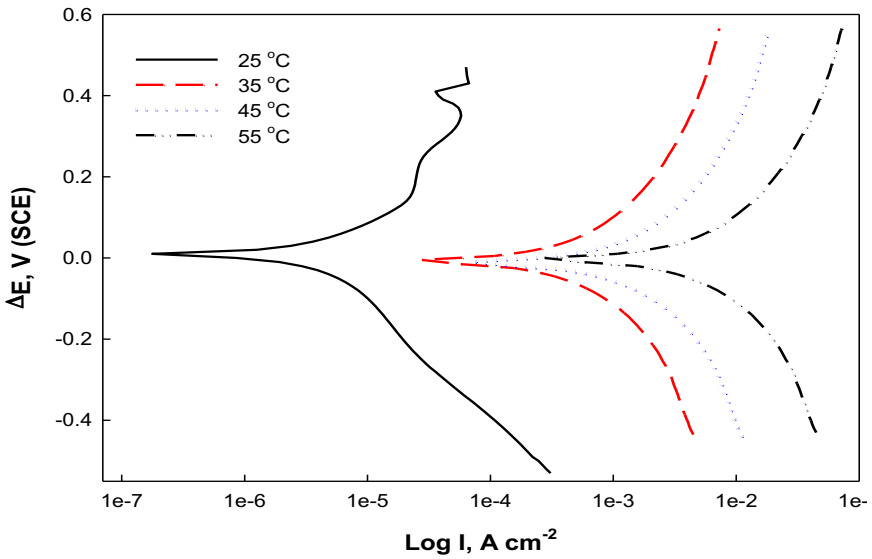

Figure 12. Polarization Tafel lines of Ni/mild steel in 0.06 M citric acid solution at different temperatures.

Table 7. Electrochemical parameters derived from Tafel lines for Ni/mild steel in 0.06M citric acid at different temperatures

Temperature	$E_{corr,}$ V (SCE)	$I_{corr,}$ (A/cm^2)	b_a (V/dec)	$-b_c$ (V/dec)	C. R. mm/y
25 °C	**-0.282**	**5.917× 10^{-5}**	**0.429**	**0.266**	**0.348**
35°C	**-0.432**	**3.5 x 10^{-4}**	**0.450**	**0.362**	**0.990**
45°C	**-0.452**	**0.00033**	**0.450**	**0.362**	**3.58**
55°C	**-0.430**	**0.00085**	**0.548**	**0.500**	**12.29**

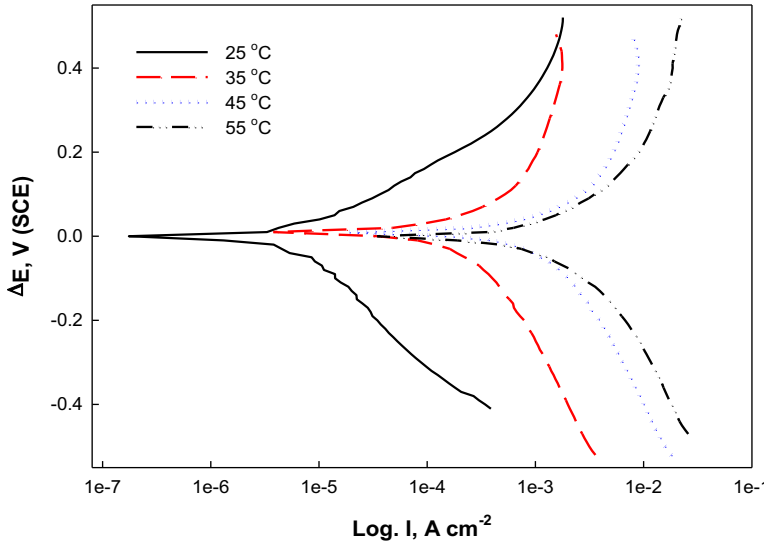

Figure 13. Polarization Tafel lines of Ni- RGO -TiO_2/mild steel (prepared at 10 mA cm^{-2} and 0.4 g L^{-1} RGO -TiO_2) in 0.06 M citric acid solution at different temperatures**.**

Table 8. Electrochemical parameters derived from Tafel lines for Ni- RGO -TiO_2/mild steel (prepared at 10 mA cm^{-2} and 0.4 g L^{-1} RGO -TiO_2) in 0.06 M citric acid at different temperatures

Temperature	$E_{corr,}$ V (SCE)	$I_{corr,}$ (A/cm^2)	b_a (V/dec)	$-b_c$ (V/dec)	C. R. mm/y
25 °C	**-0.144**	**2.52× 10^{-6}**	**0.259**	**0.255**	**0.148**
35°C	**-0.260**	**4.2x10^{-5}**	**0.570**	**0.430**	**0.452**
45°C	**-0.275**	**2.1x10^{-4}**	**0.715**	**0.473**	**2.26**
55°C	**-0.273**	**0.0003**	**0.562**	**0.421**	**3.3**

Figure 14 represents the Arrhenius plots, which relates the logarithm of the corrosion current (I_{corr}) to the reciprocal of absolute temperature (1/T), for bare, Ni-coated, and Ni–RGO–TiO_2-coated mild steel in 0.06 M citric acid. The apparent effective activation energy (E_a), which was determined from the slopes of these plot lines (**Figure 14**), amounted to 51.5, 70.4, and 131.4 kJ mol^{-1} for the corrosion reactions involving bare, Ni-coated, and Ni–RGO–TiO_2-coated mild steel, respectively, in 0.06 M citric acid. The formation of a protective barrier on the coated mild steel and the relatively high E_a value are responsible for the relatively low I_{corr} values. Overall, Ni- and Ni–RGO–TiO_2-coated mild steel exhibited low corrosion rates under the present experimental conditions.

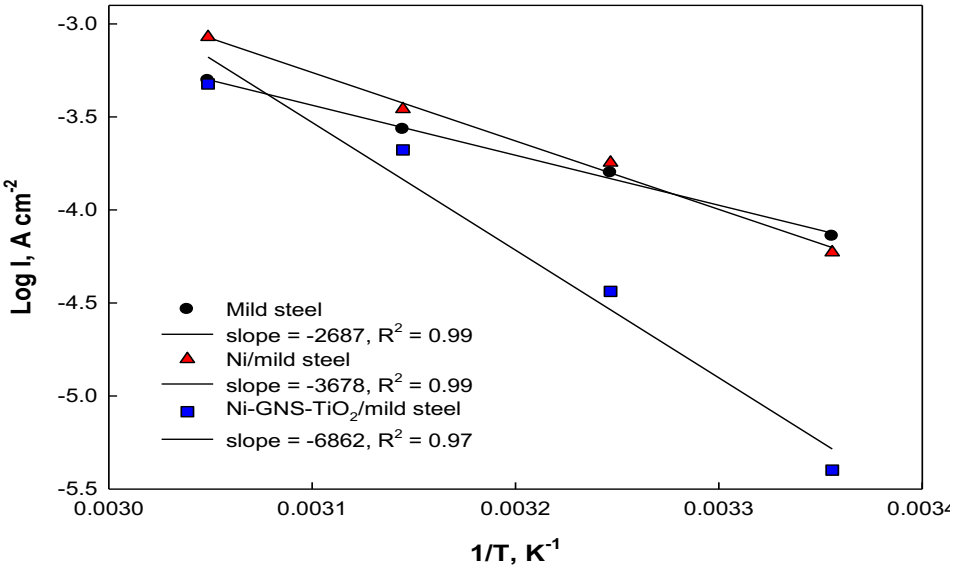

Figure 14. Log I_{corr} vs 1/T relation for mild steel, Ni/mild steel and Ni- RGO -TiO_2/mild steel (prepared at 10 mA cm^{-2} and 0.4 g L^{-1} RGO -TiO_2) in 0.06 M citric acid.

Corrosion tests in 0.1 M acetic acid

Polarization Tafel lines of bare and coated mild steel electrodes in acetic acid

Polarization Tafel plots were acquired in acetic acid for bare and coated mild steel electrodes starting from the open-circuit potential. The temperature was adjusted to the desired value using a water thermostat. **Figure 15 and Table 9** show the Tafel lines of the Ni–20.4 wt.%RGO–TiO_2-coated mild steel electrodes at different acetic acid concentrations. When the acetic acid concentration increased and, consequently, enhanced the activity of the hydrogen ions, the polarization curves shifted toward higher polarization current densities. Therefore, the acetic acid concentration was set to 0.1 M to study various samples in a corrosive medium. The corrosion rate of Ni–RGO–TiO_2-coated mild steel in acetic acid was expected to decrease with increasing acetic acid concentration because of the dissociation of acetic acid into acetate ions, which may passivate the corroding electrode by adsorption of their carboxylate groups, as described by Moussa et al. [46]. In contrast, the corrosion current increased slightly with increasing acetic acid concentration in the present work. Short-chain carboxylates could not effectively inhibit the corrosion of Ni–RGO–TiO_2-coated mild steel because they failed to completely block surface sites from anodic dissolution, which explains the observed rise in corrosion current [47].

The corrosion behaviors of the bare and coated electrodes were studied in 0.1 M acetic acid at 25 °C (**Figure 16**). **Table 10** lists the electrochemical parameters derived from the polarization Tafel lines. The Ni–RGO–TiO_2 coated mild steel samples displayed lower corrosion rates than their bare and Ni-coated equivalents. These corrosion rates decreased with increasing RGO–TiO_2content in the prepared electrode and reached their minimum for the Ni–20.4 wt.% RGO–TiO_2 coated electrode (**Table 10**). This result could be attributed to the suitable surface morphology of the electrode surface, especially the Ni–20.4 wt.% RGO–TiO_2 coated electrode.

The corrosion of Ni–RGO–TiO_2-coated mild steel electrodes prepared at different deposition current densities was studied in 0.1 M acetic acid. The corrosion rate decreased when the deposition current density grew to 10 mA cm^{-2}(**Figure 17** and **Table 11**).

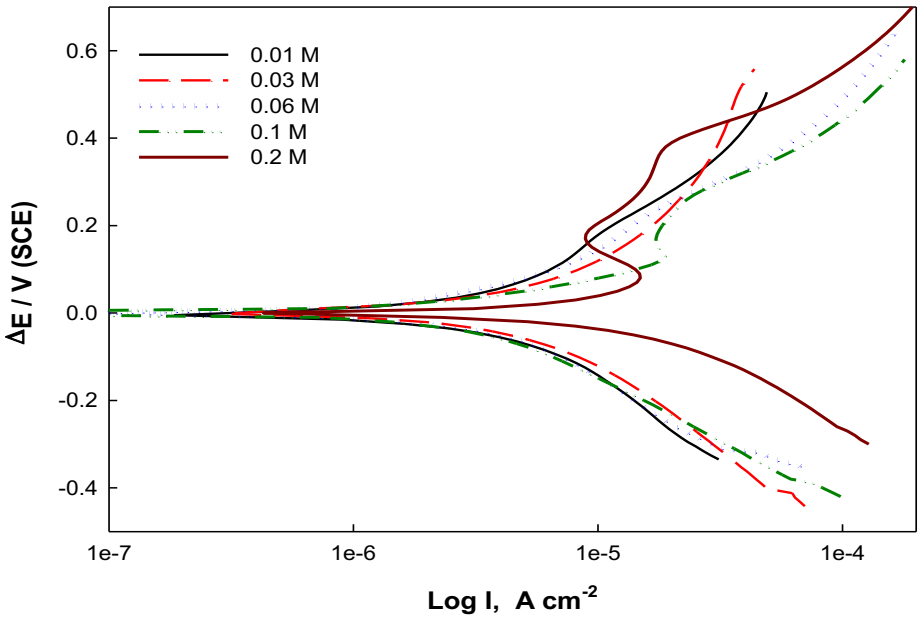

Figure 15. Polarization Tafel lines of Ni- RGO -TiO_2/mild steel (prepared at 10 mA cm^{-2} and 0.4 g L^{-1} RGO -TiO_2) in different concentrations of acetic acid solution at 25 ^oC.

Table 9. Electrochemical parameters derived from Tafel lines of Ni-RGO-TiO_2/mild steel (prepared at 10 mA cm^{-2} and 0.4 g L^{-1} RGO -TiO_2) in different concentrations of citric acid

Acetic acid concentration, M	E_{corr}, V (SCE)	I_{corr}, A cm^{-2}	b_a, V dec^{-1}	$-b_c$, V dec^{-1}	C.R mm/y
0.01	-0.124	4.573×10-6	0.444	0.418	0.269
0.03	-0.116	7.661×10-6	0.722	0.414	0.451
0.06	-0.138	3.581×10-6	0.313	0.357	0.210
0.1	-0.203	3.21 x10-6	0.295	0.291	0.189
0.2	-0.060	5.60x10-6	0.370	0.319	0.33

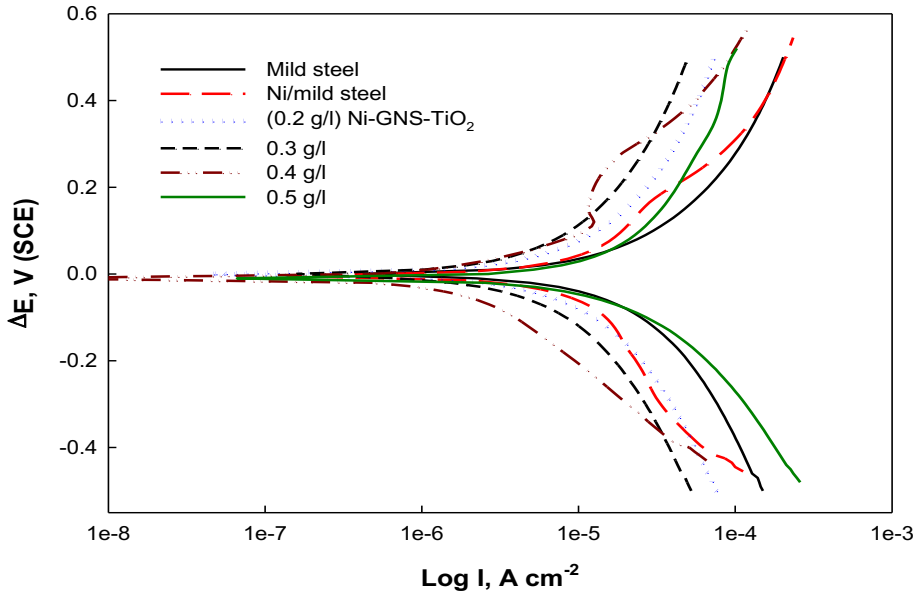

Figure 16. Polarization Tafel lines of mild steel, Ni/mild steel and Ni- RGO -TiO_2/mild steel (prepared at different concentration of RGO-TiO_2 and at 10 mA cm^{-2}) in 0.1 M acetic acid solution.

Table 10. Electrochemical parameters derived from Tafel lines for mild steel, electrodeposited Ni/mild steel and Ni-RGO-TiO_2/mild steel contains different concentration of RGO-TiO_2 nanocomposite (deposited at 10 mA cm^{-2}) in 0.1 M acetic acid at 25 °C

Sample	RGO -TiO_2 in the bath, g L^{-1}	E_{corr}, V (SCE)	I_{corr}, (A/cm^2)	b_a (V/dec)	$-b_c$ (V/dec)	C. R. mm/y
Mild Steel	-	**-0.585**	**2.395×10^{-5}**	**0.483**	**0.572**	**1.41**
Ni/mild steel	-	**-0.358**	**1.104×10^{-5}**	**0.553**	**0.337**	**0.701**
Ni-RGO-TiO_2 (I)	**0.2**	**-0.50**	**1.06×10^{-5}**	**0.570**	**0.569**	**0.626**
Ni-RGO-TiO_2 (II)	**0.3**	**-0.511**	**1.011×10^{-5}**	**0.545**	**0.556**	**0.595**
Ni-RGO-TiO_2 (III)	**0.4**	**-0.203**	**3.21×10^{-6}**	**0.295**	**0.291**	**0.189**
Ni-RGO-TiO_2 (IV)	**0.5**	**-0.392**	**2.126×10^{-5}**	**0.626**	**0.429**	**1.252**

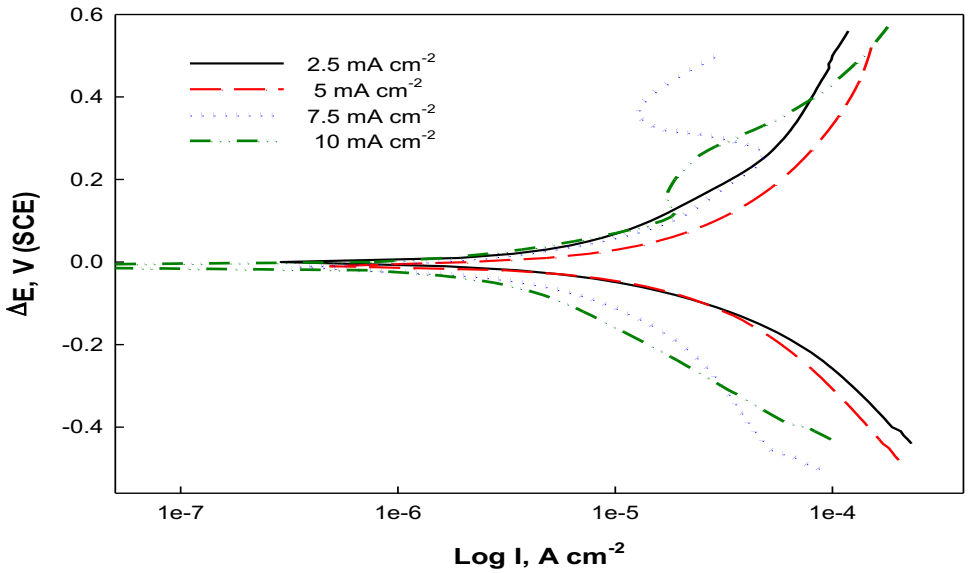

Figure 17. Polarization Tafel lines of Ni- RGO -TiO_2/mild steel (prepared at different deposition current densities and at 0.4 g L^{-1} RGO -TiO_2) in 0.1 M acetic acid solution

Table 11. Electrochemical parameters derived from Tafel lines of Ni- RGO -TiO_2/mild steel (prepared at different deposition current densities and 0.4 g L^{-1} RGO -TiO_2 nanocomposite in the bath) in 0.1 M acetic acid at 25 °C.

Sample at cd ($mA\ cm^{-2}$)	E_{corr} V (SCE)	I_{corr} (A/cm^2)	b_a (V/dec)	$-b_c$ (V/dec)	C.R. (mm/y)
2.5	**-0.060**	**4.503×10^{-5}**	**0.595**	**0.455**	**0.599**
5	**-0.400**	**2.44×10^{-5}**	**0.583**	**0.470**	**0.470**
7.5	**-0.295**	**8.763×10^{-6}**	**0.541**	**0.386**	**0.386**
10	**-0.203**	**3.21×10^{-6}**	**0.295**	**0.291**	**0.189**

Electrochemical impedance spectroscopy in 0.1 M acetic acid

The corrosion resistance of bare and coated steel samples in 0.1 M acetic acid was evaluated by EIS at applied frequencies ranging from 35 kHz to 100 MHz (**Figures 18 and 19** and **Tables 12 and 13**). The resulting Nyquist plots showed a straight line (Warburg) in the low-frequency region and one capacitive loop in the high-frequency region (**Figures 18 and 19**). The capacitive loop is assigned to R_{ct}, whereas the W impedance results from the propagation of the cathodic and anodic reaction products from the solution to the electrode surface. The Ni–RGO–TiO_2-coated mild steel electrodes presented substantially higher EIS-derived R_p values than bare and Ni-coated equivalents. These R_p values increased with increasing RGO–TiO_2 nanocomposite content in the composite electrode to reach a maximum for a RGO–TiO_2 composition of 20.4 wt.%, demonstrating the high corrosion resistance of the nanocomposite coating. The decrease in electrolyte penetration into the steel surface

resulted from the presence of a protective coating film, which provided a diffusion barrier. The R_p values also increased when the deposition current density increased. This electrochemical behavior was represented by the same equivalent electrical circuit model Rs(RpW)C) as in 0.06 M citric acid (**Figure 10**).

The capacity values of the Ni–RGO–TiO_2-coated mild steel electrode decreased when Rp values increased. This may result from the appropriate coverage of the electrodes by the coatings, which produced a barrier against diffusion. Impedance parameters were calculated for various nanocomposite-coated mild steel electrodes (**Tables12 and 13**). Based on the N values, the results are in good agreement with the data obtained from the Tafel lines. The best R_p value was recorded for a coating presenting a relatively higher RGO–TiO_2nanocomposite content. Bare, Ni-coated, and Ni–20.4 wt.% RGO–TiO_2/mild steel electrodes displayed R_p values of 0.61, 6.1, and 64 KΩ cm^2, respectively.

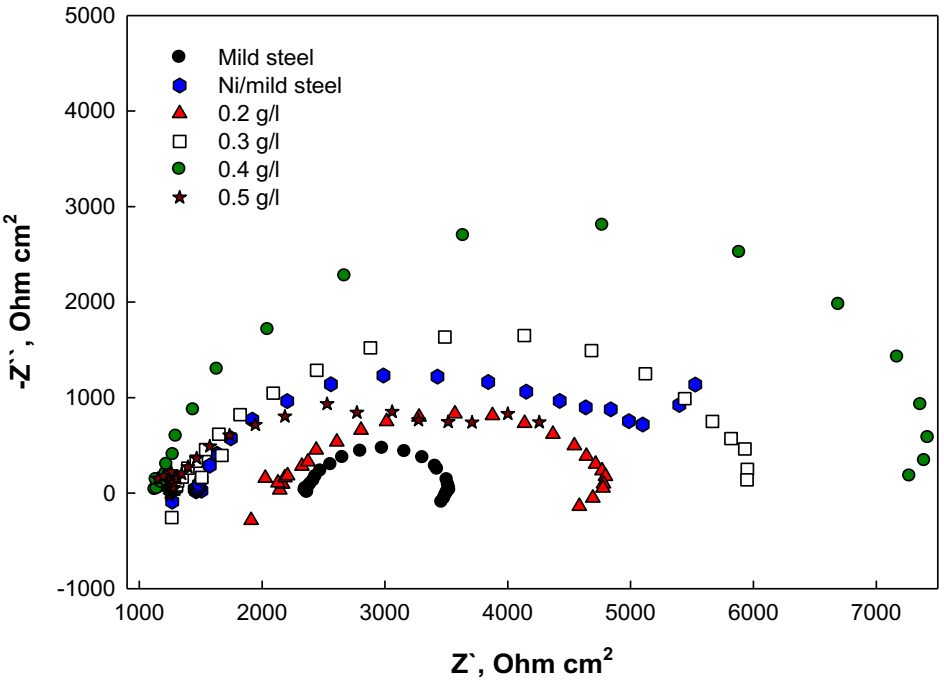

Figure 18. Nyquist plots for Ni- RGO -TiO_2/mild steel electrodes (prepared at different concentrations of RGO -TiO_2 and at 10 mA cm^{-2}) in 0.1 M acetic acid at open circuit potential.

Table 12. Electrochemical parameters derived from EIS for mild steel, Ni/mild steel and Ni- RGO -TiO_2/mild steel (prepared at different concentrations of RGO -TiO_2 nanocomposite in the bath and at 10 mA cm^{-2}) in 0.1 M acetic acid at 25 °C

Conc.of RGO -TiO_2(g L^{-1})	R_1, Ohm cm^2	R_2, Ohm cm^2	C, F cm^2	W, Ohm cm^2	n
Steel	**2.453× 10^3**	**1.064× 10^3**	**3.829× 10^{-5}**	**1.050 ×10**	**0.999**
Ni/mild steel	**1.530 ×10^3**	**2.782 ×10^3**	**5.293×10^{-5}**	**3.135× 10^2**	**0.99**
0.2	**3.02x10^3**	**3.340x10^3**	**1.702x10^{-4}**	**4.78x10**	**0.97**
0.3	**1.435x10^3**	**4.000x10^3**	**2.4x10^{-4}**	**1.16x10^2**	**0.97**
0.4	**1.218x10^3**	**6.043x10^3**	**3.397x10^{-5}**	**1.073x10**	**0.999**
0.5	**1.312 ×10^3**	**2.180× 10^3**	**1.016×10^{-4}**	**1.81× 10^2**	**0.99**

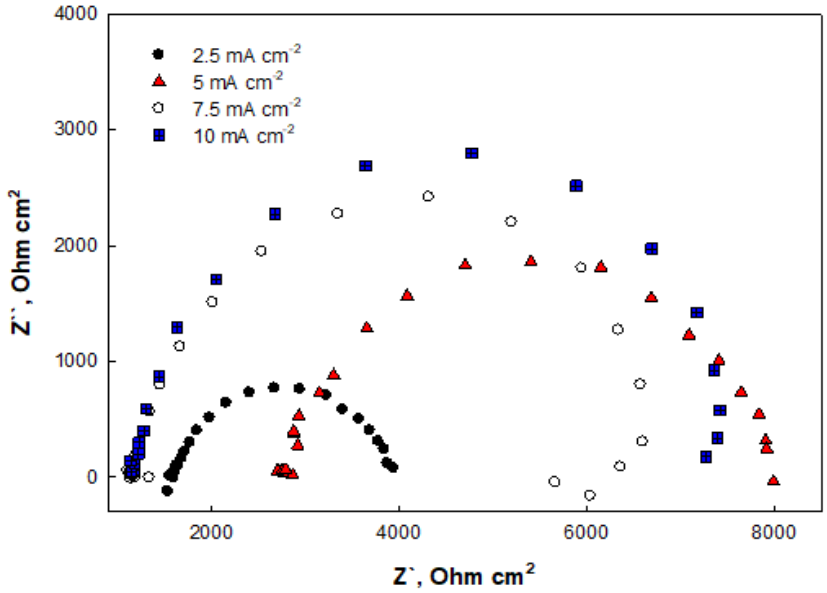

Figure 19. Nyquist plots for Ni- RGO -TiO_2/mild steel electrodes (prepared at different deposition current densities and 0.4 g L^{-1} RGO -TiO_2) in 0.1 M acetic acid at open circuit potential.

Table 13. Electrochemical parameters derived from EIS for Ni- RGO -TiO_2/mild steel (prepared at different deposition current densities and 0.4 g L^{-1} RGO -TiO_2 nanocomposite in the bath) in 0.1 M acetic acid at 25 °C

Deposition cd, mA cm^{-2}	R_1, ohm cm^2	R_2, ohm cm^2	C, F cm^2	W, ohm cm^2	n
2.5	**1.637×10^3**	**2.056×10^3**	**5.024×10^{-5}**	**8.7690**	**0.99**
5	**2.88×10^3**	**4.552×10^3**	**4.715×10^{-5}**	**1.015×10^2**	**0.99**
7.5	**1.22×10^2**	**5.048×10^3**	**1.53×10^{-5}**	**0.71×10^2**	**0.99**
10	**1.218×10^3**	**6.043×10^3**	**3.397×10^{-5}**	**1.073x10**	**0.999**

The influence of temperature on the corrosion of bare, Ni-coated, and Ni–20.4 wt.% RGO–TiO_2-coated mild steel electrodeswas studied in 0.1 M acetic acid between 25and 55 °C (**Figures 20–22** and **Tables14–16**). For all samples, the corrosion rate increased with temperature. This behavior could be explained by thetemperature-related acceleration of all other processes involved in corrosion, such as chemical reactions, electrochemical reactionsand reactive species transfer to the electrode surface[48].

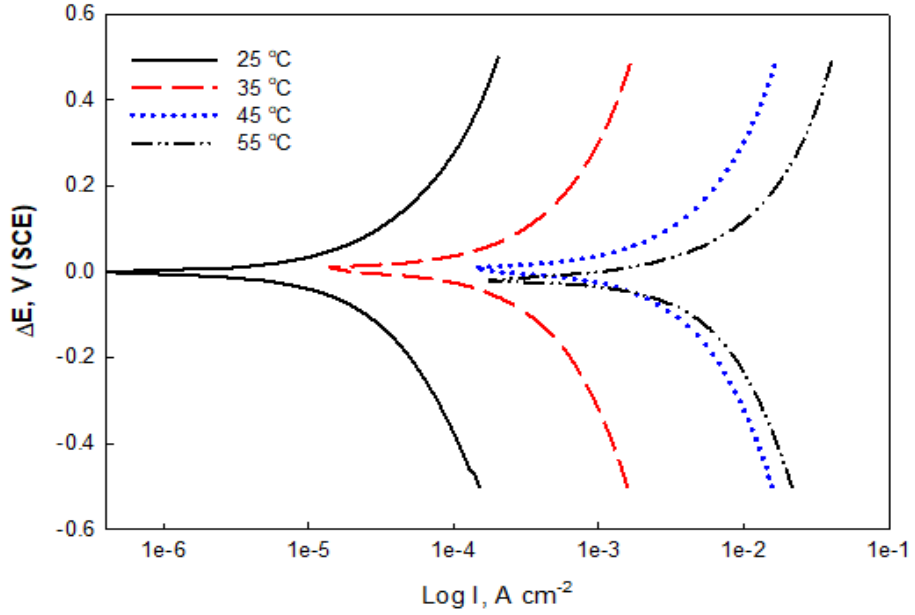

Figure 20. Polarization Tafel lines of mild steel in 0.1 M acetic acid solution at different temperatures.

Table 14. Electrochemical parameters derived from Tafel lines for mild steel in 0.1 M acetic acid at different temperatures

Temperature, °C	E_{corr}, V (SCE)	I_{corr}, (A/cm^2)	b_a (V/dec)	$-b_c$ (V/dec)	C. R. mm/y
25	**-0.585**	**2.395× 10^{-5}**	**0.483**	**0.572**	**1.41**
35	**-0.600**	**3.01x10^{-5}**	**0.511**	**0.589**	**1.766**
45	**-0.612**	**2.9 x10^{-4}**	**0.561**	**0.636**	**3.82**
55	**-0.579**	**5.7 x10^{-4}**	**0.594**	**0.664**	**7.36**

Table 15. Electrochemical parameters derived from Tafel lines for Ni/mild steel in 0.1 M acetic acid at different temperatures

Temperature, °C	E_{corr}, V (SCE)	I_{corr}, (A/cm^2)	b_a (V/dec)	$-b_c$ (V/dec)	C. R. mm/y
25	**-0.358**	**1.104 ×10^{-5}**	**0.553**	**0.337**	**0.701**
35	**-0.341**	**1.31x10^{-5}**	**0.564**	**0.342**	**0.831**
45	**-0.262**	**1.27 x10^{-4}**	**0.819**	**0.961**	**1.36**
55	**-0.476**	**3.8 x10^{-4}**	**0.484**	**0.567**	**4.05**

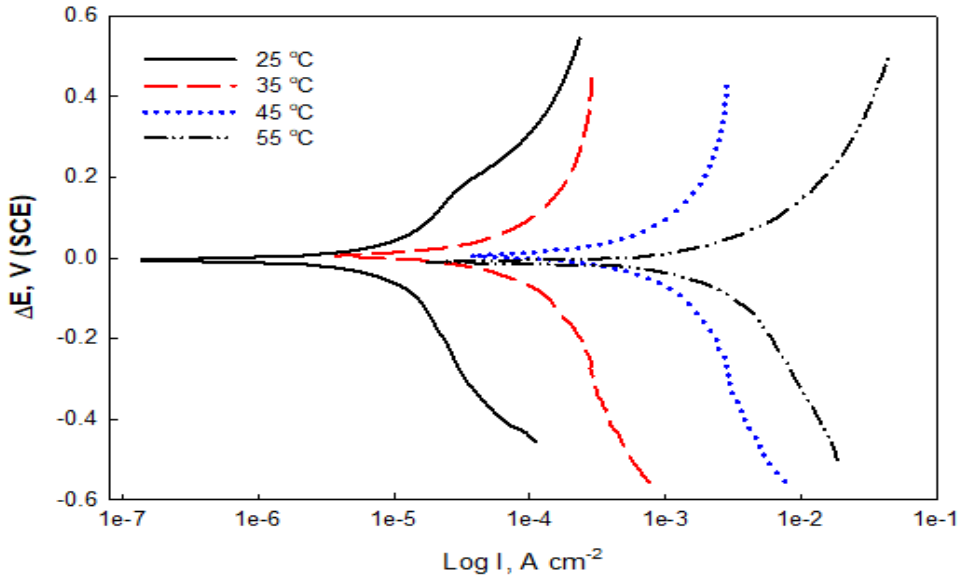

Figure 21. Polarization Tafel lines of Ni/mild steel in 0.1 M acetic acid solution at different temperatures.

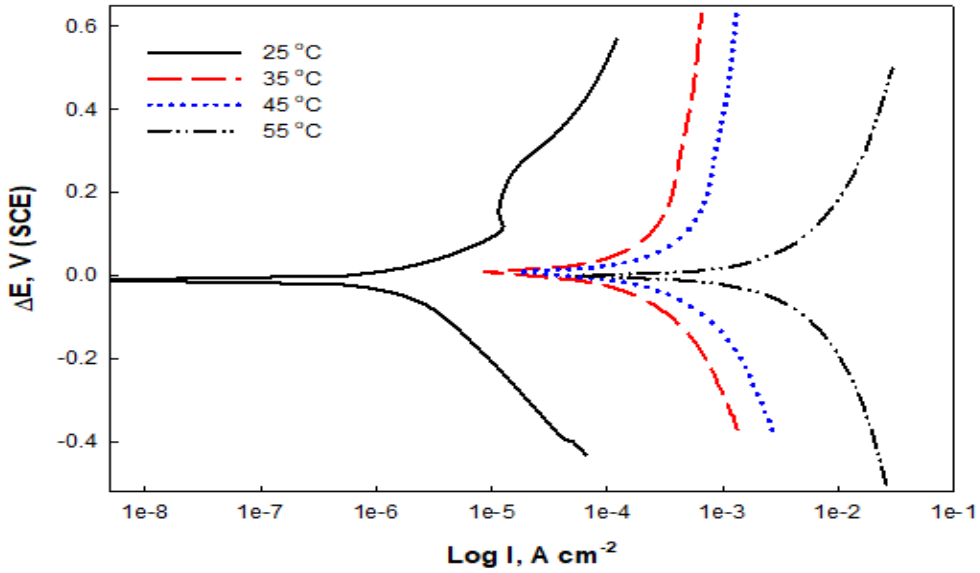

Figure 22. Polarization Tafel lines of Ni- RGO -TiO_2/mild steel (prepared at 10 mA cm^{-2} and 0.4 g L^{-1} RGO -TiO_2) in 0.1 M acetic acid solution at different temperatures.

Table 16. Electrochemical parameters derived from Tafel lines for Ni- RGO -TiO_2/mild steel (prepared at 10 mA cm^{-2} and 0.4 g L^{-1} RGO -TiO_2) in 0.1 M acetic acid at different temperatures

Temperature	$E_{corr,}$ V (SCE)	$I_{corr,}$ (A/cm^2)	b_a (V/dec)	$-b_c$ (V/dec)	C. R. mm/y
25 °C	**-0.203**	**3.21×10^{-6}**	**0.295**	**0.291**	**0.189**
35 °C	**-0.226**	**2.52×10^{-5}**	**0.856**	**0.476**	**0.234**
45 °C	**-0.232**	**5.33×10^{-5}**	**0.867**	**0.472**	**0.569**
55 °C	**-0.491**	**4.9×10^{-4}**	**0.553**	**0.630**	**5.29**

Figure 23 shows the Arrhenius plotsfor bare, Ni-coated, and Ni–20.4 wt.% RGO–TiO_2-coated mild steel electrodes. The E_a values amounted to 84.7, 109, and 123.6 kJ mol^{-1} for the corrosion reactions in 0.1 M acetic acid of bare, Ni-coated, and Ni–20.4 wt.%RGO–TiO_2-coated mild steel electrodes, respectively.

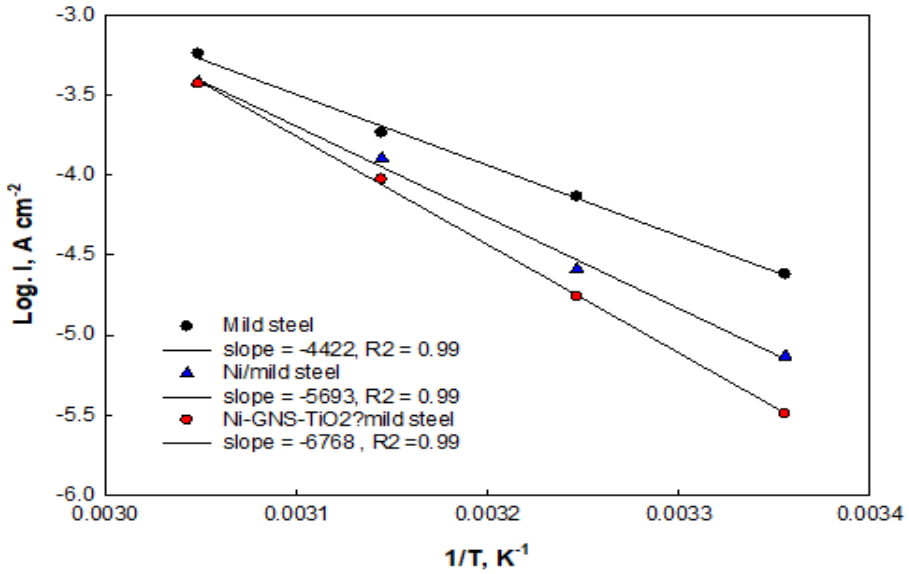

Figure 23.Log I_{corr} vs 1/T relation for mild steel, Ni/mild steel and Ni- RGO -TiO_2/mild steel (prepared at 10 mA cm^{-2} and 0.4 g L^{-1} RGO -TiO_2) in 0.1 M acetic acid.

The formation of a protective barrier in the case of Ni- and Ni–RGO–TiO_2-coated mild steel and the relatively high E_a value are responsible for the relatively low I_{corr} values. On the whole, Ni- and Ni–RGO–TiO_2-coated mild steel displayed low corrosion rates under the present experimental conditions.

Conclusions

In summary, a RGO–TiO_2nanocomposite was synthesized by a hydrothermal method and characterized using various techniques. The nanocomposite was incorporated in a Ni–RGO–TiO_2 coating, which was prepared on mild steel by electrodeposition. The inclusion of RGO-TiO_2 nanocomposite particles into the Ni coating enhanced the corrosion resistance of mild steel compared to Ni alone. The corrosion rate in 0.06 M citric acid and 0.1 M acetic acid increased with successive increases in the solution temperature.

References

1. S. Kirtay, Preparation of Hybrid Silica Sol–Gel Coatings on Mild Steel Surfaces and Evaluation of Their Corrosion Resistance, *Prog. Org. Coat.,* 77 (2014) 1861-1866.
2. P.R. Roberge, Corrosion Monitoring, Corrosion Inspection and Monitoring, John Wiley & Sons, Inc.2007, pp. 189-316.
3. S.K. Singh, A.K. Mukherjee, M.M. Singh, Corrosion Behaviour of Mild Steel in Aqueous Acetic Acid Solutions Containing Different Amounts of Formic Acid, *Indian J. Chem. Technol.*, 18 (2011) 291-300.
4. J. Amri, E. Gulbrandsen, R.P. Nogueira, Pit Growth and Stifling on Carbon Steel in CO_2-Containing Media in The presence of HAc, *Electrochim. Acta,* 54 (2009) 7338-7344.

5. P. Molera, F. Sanz-Soro, J.J. Suñol, The corrosion Resistance of A Fe/Cu Composite, *Mater. Corros.*, 57 (2006) 568-572.
6. A.R. Elkais, M.M. Gvozdenović, B.Z. Jugović, B.N. Grgur, The influence of Thin Benzoate-Doped Polyaniline Coatings on Corrosion Protection of Mild Steel in Different Environments, *Prog. Org. Coat.*, 76 (2013) 670-676.
7. M.W. Khalil, T.A. Salah Eldin, H.B. Hassan, K. El-Sayed, Z. Abdel Hamid, Electrodeposition of Ni–GNS–TiO_2 Nanocomposite Coatings as Anticorrosion Film for Mild Steel in Neutral Environment, *Surf. Coat. Technol.,* 275 (2015) 98-111.
8. Z. Abdel Hamid, H.B. Hassan, Influence of Electrodeposition Parameters on The characteristics of NiMoP Film, *Surf. Coat. Technol.,* 212 (2012) 37-45.
9. Z.A. Hamid, H.B. Hassan, A.M. Attyia, Influence of Deposition Temperature and Heat Treatment on The performance of Electroless Ni–B Films, *Surf. Coat. Technol.,* 205 (2010) 2348-2354.
10. C.M. Praveen kumar, T.V. Venkatesha, K.G. Chandrappa, Effect of Surfactants on Co-deposition of B4C Nanoparticles in Zn Matrix by Electrodeposition and its Corrosion Behavior, *Surf. Coat. Technol.,* 206 (2012) 2249-2257.
11. Corrosionpedia, Corrosion Protection Method, 2017.
12. Y.H. Ahmad, A.M.A. Mohamed, Electrodeposition of Nanostructured Nickel-Ceramic Composite Coatings: A review, *Int. J. Electrochem. Sci.,* 9 (2014) 1942-1963.
13. L. Shi, C.F. Sun, F. Zhou, W.M. Liu, Electrodeposited Nickel–Cobalt Composite Coating Containing Nano-sized Si_3N_4, *Mater. Sci. Eng.* A, 397 (2005) 190-194.
14. F.A. Lowenheim, S. American Electroplaters, Electroplating, McGraw-Hill1978.
15. C. Zhou, X. Lu, Z. Xin, J. Liu, Y. Zhang, Polybenzoxazine/SiO_2 Nanocomposite Coatings for Corrosion Protection of Mild Steel, *Corros. Sci.,* 80 (2014) 269-275.
16. F. Chen, P. Liu, Conducting Polyaniline Nanoparticles and Their Dispersion for Waterborne Corrosion Protection Coatings, *ACS Appl. Mater. Interfaces,* 3 (2011) 2694-2702.
17. X. Shi, T.A. Nguyen, Z. Suo, Y. Liu, R. Avci, Effect of Nanoparticles on The anticorrosion and Mechanical Properties of Epoxy Coating, *Surf. Coat. Technol.,* 204 (2009) 237-245.
18. H. Shi, F. Liu, L. Yang, E. Han, Characterization of Protective Performance of Epoxy Reinforced with Nanometer-Sized TiO_2 and SiO_2, *Prog. Org. Coat.,* 62 (2008) 359-368.
19. C.R. Raghavendra, S. Basavarajappa, S. Irappa, Electrodeposition of Ni-Al_2O_3 Nanocomposite Coating and Evaluation of Wear Characteristics, *IOP CONF. SER. MATER. SCI.,* 149 (2016) 012110.
20. S. Iijima, Helical Microtubules of Graphitic Carbon, *Nature,* 354 (1991) 56-58.
21. K.S. Novoselov, A.K. Geim, S.V. Morozov, D. Jiang, Y. Zhang, S.V. Dubonos, I.V. Grigorieva, A.A. Firsov, Electric Field Effect in Atomically Thin Carbon Films, Science, 306 (2004) 666.
22. S.V. Harb, S.H. Pulcinelli, C.V. Santilli, K.M. Knowles, P. Hammer, A Comparative Study on Graphene Oxide and Carbon Nanotube Reinforcement of PMMA-Siloxane-Silica Anticorrosive Coatings, ACS Appl. Mater. Interfaces, 8 (2016) 16339-16350.
23. C.M.P. Kumar, T.V. Venkatesha, R. Shabadi, Preparation and Corrosion Behavior of Ni and Ni–Graphene Composite Coatings, Mater. Res. Bull., 48 (2013) 1477-1483.
24. H.-P. Huang, J.-J. Zhu, Preparation of Novel Carbon-Based Nanomaterial of Graphene and its Applications Electrochemistry, Chin. J. Anal. Chem., 39 (2011) 963-971.
25. C.-T. Hsieh, W.-Y. Chen, Water/Oil Repellency and Work of Adhesion of Liquid Droplets on Graphene Oxide and Graphene Surfaces, Surf. Coat. Technol., 205 (2011) 4554-4561.
26. J. Li, Y. Sun, X. Sun, J. Qiao, Mechanical and Corrosion-Resistance Performance of Electrodeposited Titania–Nickel Nanocomposite Coatings, Surf. Coat. Technol., 192 (2005) 331-335.
27. H.M.A. Hassan, V. Abdelsayed, A.E.R.S. Khder, K.M. AbouZeid, J. Terner, M.S. El-Shall, S.I. Al-Resayes, A.A. El-Azhary, Microwave Synthesis of Graphene Sheets Supporting Metal Nanocrystals in Aqueous and Organic Media, J. Mater. Chem., 19 (2009) 3832-3837.
28. P.V. Kamat, Graphene-Based Nanoarchitectures. Anchoring Semiconductor and Metal Nanoparticles on A two-Dimensional Carbon Support, J. Phys. Chem. Lett., 1 (2009) 520-527.

29. B. Szeptycka, A. Gajewska-Midzialek, T. Babul, Electrodeposition and Corrosion Resistance of Ni-Graphene Composite Coatings, J. Mater. Eng. Perform., 25 (2016) 3134-3138.
30. Q. Liu, J. Shi, L. Zeng, T. Wang, Y. Cai, G. Jiang, Evaluation of Graphene as an Advantageous Adsorbent for Solid-Phase Extraction with Chlorophenols as Model Analytes, *J. Chromatogr. A,* 1218 (2011) 197-204
31. W.S. Hummers, R.E. Offeman, Preparation of Graphitic Oxide, J. Am. Chem. Soc., 80 (1958) 1339-1339.
32. J. Yan, Z. Fan, T. Wei, W. Qian, M. Zhang, F. Wei, Fast and Reversible Surface Redox Reaction of Graphene–MnO_2 Composites as Supercapacitor Electrodes, Carbon, 48 (2010) 3825-3833.
33. Z. Hu, Y. Huang, S. Sun, W. Guan, Y. Yao, P. Tang, C. Li, Visible Light Driven Photodynamic Anticancer Activity of Graphene Oxide/TiO_2 hybrid, Carbon, 50 (2012) 994-1004.
34. Y. Ding, Q. Liao, S. Liu, H. Guo, Y. Sun, G. Zhang, Y. Zhang, Reduced Graphene Oxide Functionalized with Cobalt Ferrite Nanocomposites for Enhanced Efficient and Lightweight Electromagnetic Wave Absorption, Scientific reports, 6 (2016) 32381.
35. X.-Y. Peng, X.-X. Liu, D. Diamond, K.T. Lau, Synthesis of Electrochemically-Reduced Graphene Oxide Film with Controllable Size and Thickness and its Use in Supercapacitor, Carbon, 49 (2011) 3488-3496.
36. S. Liu, C. Liu, W. Wang, B. Cheng, J. Yu, Unique Photocatalytic Oxidation Reactivity and Selectivity of TiO_2-Graphene Nanocomposites, Nanoscale, 4 (2012) 3193-3200.
37. Q. Xiang, J. Yu, M. Jaroniec, Enhanced Photocatalytic H_2-Production Activity of Graphene-Modified Titania Nanosheets, Nanoscale, 3 (2011) 3670-3678.
38. A. Ferrari, J. Robertson, Interpretation of Raman Spectra of Disordered and Amorphous Carbon, Phys. Rev. B, 61 (2000) 14095-14107.
39. K.E.-S.M. El-Sayed, Synthesis and Characterization of Graphene Nanocomposite Coatings as Anticorrosion Material for Mild Steel Used in Agricultural Applications, Chemistry, Cairo University, Faculty of Scinece, 2015, pp. 173.
40. L. Gu, J. Wang, H. Cheng, Y. Zhao, L. Liu, X. Han, One-Step Preparation of Graphene-Supported Anatase TiO_2 with Exposed {001} Facets and Mechanism of Enhanced Photocatalytic Properties, ACS Appl. Mater. Interfaces, 5 (2013) 3085-3093.
41. M.M. Rashad, A.E. Shalan, M. Lira-Cantú, M.S.A. Abdel-Mottaleb, Enhancement of TiO_2 Nanoparticle Properties and Efficiency of Dye-Sensitized Solar Cells using Modifiers, Appl Nanosci., 3 (2013) 167-174.
42. J. Kim, W.-H. Khoh, B.-H. Wee, J.-D. Hong, Fabrication of Flexible Reduced Graphene Oxide-TiO_2 Freestanding Films for Supercapacitor Application, RSC Advances, 5 (2015) 9904-9911.
43. Y. Liu, T. Gao, H. Xiao, W. Guo, B. Sun, M. Pei, G. Zhou, One-Pot Synthesis of Rice-Like TiO_2/Graphene Hydrogels as Advanced Electrodes for Supercapacitors and The resulting Aerogels as High-Efficiency Dye Adsorbents, Electrochim. Acta, 229 (2017) 239-252.
44. H. Liu, S. Liu, Z. Zhang, X. Dong, T. Liu, Hydrothermal Etching Fabrication of TiO_2@Graphene Hollow Structures: Mutually Independent Exposed {001} and {101} Facets Nanocrystals and its Synergistic Photocaltalytic Effects, Scientific reports, 6 (2016) 33839.
45. Z. Gohari Bajestani, Y. Yurum, Synthesis of Titanium-Decorated Graphene for Renewable Energy Applications, in: I. Dincer, O.C. Colpan, O. Kizilkan, M.A. Ezan (Eds.) Progress in Clean Energy: Novel Systems and Applications, Springer, Switzerland, 2015, pp. 863-871.
46. M.N. Moussa, M.M. El-Tagoury, A.A. Radi, S.M. Hassan, Carboxylic Acids as Corrosion Inhibitors for Aluminium in Acidic and Alkaline Solutions, *Anti-Corros. Methods Mater.,* 37 (1990) 4-8.
47. U. Rammelt, S. Köhler, G. Reinhard, EIS Characterization of The inhibition of Mild Steel Corrosion with Carboxylates in Neutral Aqueous Solution, *Electrochim. Acta,* 53 (2008) 6968-6972.
48. S. Nešić, Key issues related to modelling of internal corrosion of oil and gas pipelines – A review, *Corrosion Science,* 49 (2007) 4308-4338.